Final Report

Project Title:	**High throughput CIGS solar cell fabrication via ultra-thin absorber layer with optical confinement and (Cd, CBD)-free heterojunction partner**
Project Period:	10/01/11 – 08/30/15
Project Budget:	$1,117,400
Submission Date:	11/30/15
Recipient:	Old Dominion University Research Foundation
Address:	ODURF, ODU Research Foundation, P.O. Box 6369, Norfolk, VA 23508
Award Number:	DE-EE0005400
Project Team:	Old Dominion University
	University of Illinois Urbana Champaign
	University of Toledo
Contacts:	Sylvain Marsillac Professor Phone: 757.683.6368 Email: smarsill@odu.edu

Executive Summary

The main objective of this proposal was to use several pathways to reduce the production cost of CIGS PV modules and therefore the levelized cost of energy (LCOE) associated with this technology. Three high cost drivers were identified, nominally:

1) Materials cost and availability
2) Large scale uniformity
3) Improved throughput

These three cost drivers were targeted using the following pathways:

1) Reducing the thickness of the CIGS layer while enhancing materials quality
2) Developing and applying enhanced in-situ metrology via real time spectroscopic ellipsometry
3) Looking into alternative heterojunction partner, back contact and AR coating

Eleven main Tasks were then defined to achieve these goals (5 in Phase 1 and 6 in Phase 2), with 11 Milestones and 2 Go/No-go decision points at the end of Phase 1. The key results are summarized below

For the back contact, we demonstrated enhanced current with ZrN back contact compared to Mo back contact for 0.5 um CIGS, and achieved 8.5% efficiency solar cell with Ag/Glass/TCO back contact for 0.5 um CIGS

To allow us to reduce the CIGS thickness while enhancing device quality, we implemented RTSE as an effective *in-situ* and real time tool for controlling 3-stage process deposition. We then demonstrated the influence of gallium content on the growth process and the need for controlling its content in ultra-thin films. We also demonstrated the capacity to use mapping SE to correlate extracted results with device performance. The use of nano-DLTS allowed us to identify activation energy of various trap levels, showing that they are systematically located at grain boundaries, but not present at every grain boundary. Finally we fabricated several high efficiency ultra-thin CIGS solar cells, notably a 13.2% cell for 0.73 um CIGS and a 10.4% cell for 0.55 um CIGS and a 9.1 % cell for a 0.35 um cell (baseline for these cells was 16% for 2 um CIGS). This is on par with the best ultra-thin CIGS solar cells ever reported.

For the buffer layers, we showed that alternative materials such as ZnS and InS are viable to enhance current generation, and that ALD is a good alternative to CBD deposition.

We also worked extensively on enhanced AR filters, notably by successfully depositing and modeling a variety of 2-layer, 3-layer and 4 layer AR filters based on MgF_2, HfO_2, Al_2O_3, SiO_2, ZrO_2, TiO_2, and demonstrating enhanced current generation compared to a single MgF_2 layer in all cases. We also modeled the effect of AR coating on ultra-thin CIGS solar cell efficiency using a variety of back contact and predicted QE spectrum based on SE measurements. Finally, we successfully demonstrated the capacity to use SE as a real time tool to optimize thickness of the AR filter for enhanced efficiency

These efforts resulted in 9 publications in peer-reviewed journals and 17 publications in peer-reviewed conference proceedings.

1. Background

The concept of thinning the Cu(In,Ga)Se$_2$ (CIGS) layer is of great interest and has already been explored by several researchers [1-4]. The potential advantages of this concept derive from the reduction of cost and usage of materials (especially indium and gallium) and the increase in production throughput. In a standard CIGS device, the absorber thickness is typically 2.5 µm. Thickness of the absorbing layer reduction down to 0.5 µm would save 80% of the semiconductor material by considering the same yield and the deposition time would be five times shorter by keeping the same deposition rate. Some significant achievements for producing ultra-thin cells with good performance are shown in Figure 1.1. More recently, recorded best CIGS solar cell [5] (blue diamond in Figure 1) have shown significant improvement in voltage and fill-factor. The thin films of the recent ultra-thin devices are smoother, making it possible to produce 0.5 µm or thinner devices. The thinnest device (0.15 µm) with remarkable performance [4] is 5 % efficient. The best 1 µm CIGS device [6] has achieved efficiency of 17.1 %, which is only 4.6 % less than the record CIGS solar cell [5]. Even though the thin CIGS solar cells have shown remarkable improvement in open circuit voltage (V_{oc}) and fill factor (FF), current reduction still remains which is the main cause for the thin film solar cells' lower efficiency.
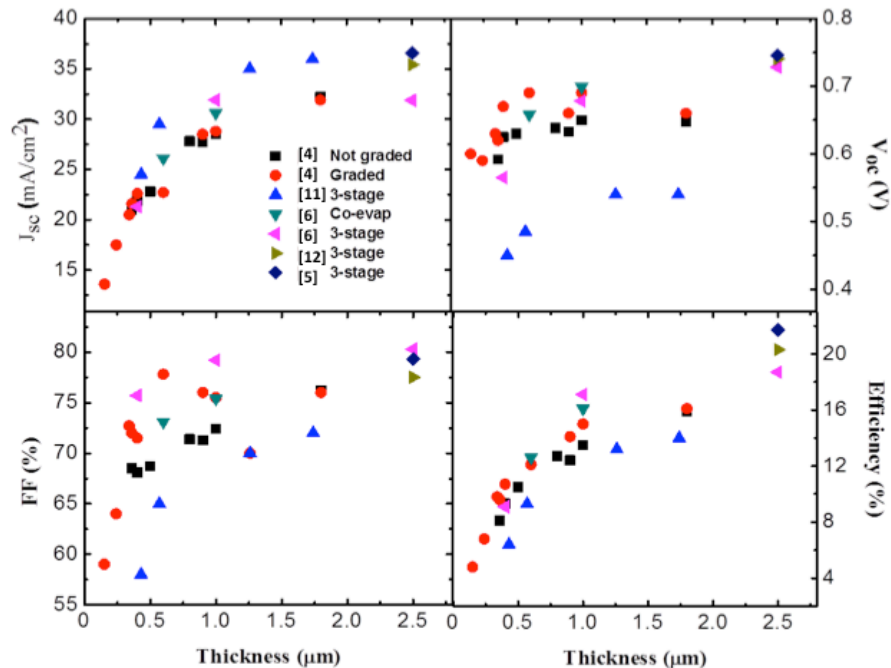

Figure 1.1. Review of experimental results of CIGS solar cells with thin absorbers layers (references in parenthesis)

Several new papers have been published on the topic this year (2015), indicating a continuous interest in the subject [7-10]. It involves notably the deposition of an Al$_2$O$_3$ layer to passivate the back contact and use Mo nano-particles as local rear-contact [7]. This enhanced the current but decrease the overall cell efficiency. Deposition of ultra-thin cell by ALD at low temperature results in low efficiency of 2.6% [8]. Patterning the back contact with TiO$_2$ or SiO$_2$ nanoparticle allows the enhancement of the current and efficiency up to 12.3% to be achieved for thickness of 460 nm [9]. Finally, reducing the deposition temperature down to 440°C for a 500 nm cell is shown to potentially enhance current collection as the Ga profile is modified, allowing efficiency of 10.6% to be reached [10].

2. Introduction

2.1. Significance

The main objective of this proposal was to use several pathways to reduce the production cost of CIGS PV modules and therefore the levelized cost of energy (LCOE) associated with this technology. Three high cost drivers were identified, nominally:

4) Materials cost and availability
5) Large scale uniformity
6) Improved throughput

These three cost drivers were targeted using the following pathways:

4) Reducing the thickness of the CIGS layer while enhancing materials quality
5) Developing and applying enhanced in-situ metrology via real time spectroscopic ellipsometry
6) Looking into alternative heterojunction partner, back contact and AR coating

2.2. Innovation

The structure of the solar cell used in our work was Substrate / Back Contact + Reflector / CIGS / Junction Partner / Front Contact / Grids /AR Filter. The approaches to enhance each of them to achieve our objectives were as follows:

2.2.1. Back Contact + Reflector

The constraints on the back contact of the CIGS solar cell are numerous: we can cite most notably an ohmic contact with CIGS, chemical inertness in the deposition process (500°C under Se atmosphere), and reasonable thermal expansion match. A wide variety of materials have been attempted for the back contact of CIGS solar cells (e.g. W, Mo, Cr, Ta, Nb, V, Ti, Mn), but none has been as successful as Mo. Problems encountered with other contacts range from reaction with Se to lack of back surface passivation. One of the problems associated with Mo for our specific structure, however, is that it does not serve as a good reflector for the red and near-infrared photons. Here too, several materials have been attempted to enhance back reflection, such as TiN or ZrN, but another problem then arises: the lack of good ohmic contact with CIGS. A thin layer, of $MoSe_2$ for example, must then be introduced to restore the ohmicity, which defeats the purpose of the enhanced reflector. As an alternative, transparent conductive oxides have been incorporated at deposition temperatures of 500°C or less. ITO and SnO_2:F have been successful in this application, whereas ZnO:Al has not. We therefore proposed a two pronged approach to enable deposition of a stable and ohmic back contact, while enhancing the back reflection:

(i) A back reflector based on a TCO in conjunction with a mirror below it
(ii) Alloys with good conductivity and high red and near-IR reflectivity based on transition metal nitride alloys

2.2.2. CIGS Layer

The CIGS was deposited by thermal co-evaporation via a 2 or 3 stage process. The main change for this layer was to thin it down to 0.25 μm while maintaining good material quality. This control and enhancement of the quality was realized by modification of the deposition process via in-situ and real time feedback from spectroscopic ellipsometry (RTSE). Among the tools we considered for growth modification were temperature profiling, modified back contact, amount of Na introduced during growth and band gap profiling.

2.2.3. Junction Partner
We looked at alternative to CBD-deposited CdS as the heterojunction partner, by using alternative deposition process (ALD) or alternative materials (ZnS, InS).

2.2.4. AR Filter
It is critical to enhance the current by using a back reflector and an anti-reflection (AR) coating working in tandem to trap the light inside the cell. To this effect, there are three options: (i) random forward scattering via a textured front contact with a single AR coating, (ii) random scattering via back surface nano-structure (as mentioned in the introduction), and (iii) an advanced multilayer stack for AR on top of a smooth front contact. We chose to develop the later solution, by using topside multilayer coatings that operate in conjunction with the back-reflector to serve as a light trap in the red and near-infrared where enhanced absorption is required. The goal was to achieve at least five passes in internal reflection for complete absorption of above gap light. Two main solutions were proposed:

  (i) Multilayer AR coating made of layers of various refractive indexes
  (ii) Multilayer AR coating made of High/Low index profile

2.3. Summary of the main Tasks to be performed according to the SOPO
2.3.1. Budget Period I
Task #1 – *Back Contact (Quarter 1-Quarter 6)*
The project team will focus on depositing new back contact materials, taking into account potential problems with the work function of the materials, the ohmicity of the contact, adhesion and the chemical inertness during the subsequent deposition process. The project team will also study the influence of sodium. This project phase consists of *3 subtasks*.

I.1.1 Subtask 1: Deposit 3 types of back contacts based on a 1st compound. Fabricate solar cells with 2 and 0.5 μm CIGS.

Deliverable: 2 and 0.5 μm CIGS solar cells with 3 types of back contacts based on 1st compound.

I.1.2 Subtask 2: Deposit 3 types of back contacts based on 2nd compound. Fabricate solar cells with 2 and 0.5 μm CIGS.

Deliverable: 2 and 0.5 μm CIGS solar cell with 3 types of back contacts based on 2nd compound. Compare Voc and FF to reference Mo cell.

I.1.3 Subtask 3: The influence of sodium on the CIGS solar cell is critical. Without it, high efficiency solar cells would not be achieved even for thick CIGS, making it even more crucial in this case. The project team will therefore deposit various amount of sodium compounds (e.g. NaF) before, during and after the growth of the CIGS and see its influence on device parameters and growth.

Deliverable: 2 and 0.5 μm CIGS solar cell with back contacts based on 1st and 2nd compound.

Task #2 – *Thickness (Quarter 1-Quarter 6)*
RTSE will be used as the main tool to evaluate the growth process while several approaches are considered for growth modification with the goal being low void density and smooth surfaces in order to avoid shunts in thin layers. In this Phase 1, the project team will deposit 0.5 μm CIGS and modify the deposition process for high quality material.

*Deliverable***:** 0.5 μm CIGS solar cell with baseline structure and demonstrated enhanced efficiency compared to efficiency on same device before modified process

Task #3 – *CBD and CdS free buffer layer (Quarter 1-Quarter 6)*
The project team will develop a Cd-free and CBD-free process for forming the heterojunction,

allowing for both conduction and valence band offsets to be controlled, depending on the absorber layer. Three types of deposition processes will be used. In this Phase 1, the project team will deposit a 1st compound by evaporation, sputtering and ALD on 2 and 0.5 μm CIGS; the project team will evaluate the effect of composition and study the effect of pre-treatment (etching, cleaning…) on the efficiency.

Deliverable: 2 and 0.5 μm CIGS solar cells with CBD and Cd-free buffer layers, achieving higher current compared to reference CdS

Task #4 – *AR Filter (Quarter 1-Quarter 6)*
In this task, the current in thin CIGS cells will by enhanced using a back reflector and an anti-reflection (AR) coating working in tandem to trap the light inside the cell. To this effect, the project team will develop top side multilayer coatings that operate in conjunction with the back-reflector to serve as a light trap in the red and near-infrared where enhanced absorption is required. The project team will deposit 3 types of AR filters on 2 and 0.5 μm CIGS solar cells, and perform optical and device characterization and modeling.

*Deliverable***:** 2 and 0.5 μm CIGS solar cells using an AR filter for enhanced efficiency compared to efficiency on same device with only MgF_2

Go/No-Go decision at the end of Phase I:
- Develop a suitable deposition process enabling fabrication of a CIGS solar cell with a 0.5 μm CIGS layer and enhanced efficiency compared to that on same device before modification of the process
- Develop a suitable buffer layer that will allow us to fabricate a solar cell with higher current compared to reference CdS

2.3.2. Budget Period II
Task #6 – *Back Contact (Quarter 7-Quarter 12)*
Identify best material and best design. Continue analysis of sodium influence. Fabricate solar cells with 2, 0.5 and 0.2 μm CIGS. Analyze (similar to Year 1) and model device parameters and reflectivity measurements.

Deliverable: 2, 0.5 and 0.2 μm CIGS solar cells with best back contact and similar efficiency compared to standard 2 μm CIGS on Mo; 0.5 and 0.2 μm CIGS with enhanced efficiency relative to thin counterparts on Mo.

Task #7 – *Thickness (Quarter 7-Quarter 12)*
Modify deposition process to enhance further material quality. Due to the low thickness the project team is trying to achieve, real-time spectroscopic ellipsometry (RTSE) will play an essential role in roughness evaluation and control. Among the other tools the project team will use to control are: sources fluxes, substrate temperature, ion bombardment of nucleation layer for the hybrid process, alloying with various elements (Ag, S…). The project team will also try to lower the surface energy by depositing a nucleation layer (Cu, Ag) at low temperature to allow for (Cu,Ag)xSe compounds to form and assist in the formation of 112 orientation, and facilitate growth with high nucleation density.

Deliverable: 2, 0.5 and 0.2 μm CIGS solar cells with enhanced deposition process, achieving improved efficiency compared to that on same device but with standard process

Task #8 – *CBD and CdS free buffer layer (Quarter 7-Quarter 12)*
This project phase consists of *2 subtasks*.
II.3.1 Subtask 1: Deposit 2nd compound junction partner by evaporation, sputtering and ALD on

2 and 0.5 μm CIGS. Evaluate effect of composition. Study the effect of pre-treatment (etching, cleaning…) on the efficiency

Deliverable: 2 and 0.5 μm CIGS solar cells with CBD and Cd-free buffer layer, achieving higher current compared to reference CdS

II.3.2 Subtask 2: Identify best material among the two families of compounds.

Deliverables: 0.2 to 2 μm CIGS solar cells with CBD and CdS free buffer layers achieving enhanced efficiency compared to device with CBD CdS

Task #9 – *AR Filter (Quarter 7-Quarter 12)*

Select best design and materials for 3 types of AR filters on 2, 0.5 and 0.2 μm CIGS solar cells. Characterize and Model the filter performance.

Deliverable: 2, 0.5 and 0.2 μm CIGS solar cells with AR filter, achieving enhanced efficiency compared to efficiency on same device with only MgF_2

Task #10 – *Full device development (Quarter 9-Quarter 12)*

Deposit 2, 0.5 and 0.25 μm CIGS solar cells with all enhancements implemented.

Deliverables: 0.2 to 2 μm CIGS solar cells with all enhancements implemented, achieving enhanced efficiency for 2 μm device and similar efficiency for the thinner structures compared to 2 μm baseline structures.

3. Project Results and Discussion

3.1. Task #1 and Task #6 – *Back Contact*

Results on these Tasks were reported in the following RPPR-2 reports

- **Report 2:** Study of ZrN contact and SnO$_2$:F contact.
- **Report 3**: Successfully deposited and characterized transition metal nitrides layers (including ZrN, TiN, ZrAlN) to be used as back contact. Demonstrated enhanced reflectance for these layers compared to molybdenum. Modeled the effect of these new back contacts on solar cell efficiency. Studied the effect of Na. Successfully fabricated CIGS solar cells with TCO spacer layer as the back contact demonstrating enhanced short circuit current. Developed modeling for the fabrication of ultra-thin CIGS solar cells using TCO back contact, metal back reflector and a 2-layer AR coating.
- **Report 4**: study SnO$_2$ back contact
- **Report 6:** study a transparent back contact with the addition of a silver layer.
- **Report 7**: study nitrides back contact
- **Report 8**: study the effect of temperature on molybdenum
- **Report 9**: study alternative back contacts, specifically with ITO and MoO$_3$

A summary of the main results can be found below

3.1.1. Nitride Back Contact

The structure of the CIGS cell using alternative back contacts is similar to the one using Mo. ZrN and VN have high reflectivity in the red or near infra-red spectrum thus exhibiting approximately 15% increase in the average reflectance when compared to using Mo as the back contact. This provides possibility of multiple passes of light through the ultra-thin CIGS layer increasing the conversion efficiency. Figure 3.1.1.a shows the reflection intensity for different back contacts. Figure 3.1.1.b compares the experimental results for reflection intensity of the CIGS device with alternative back contacts. One can see there that the quality of our nitrides is not good yet, as the reflectance is not as high as expected.
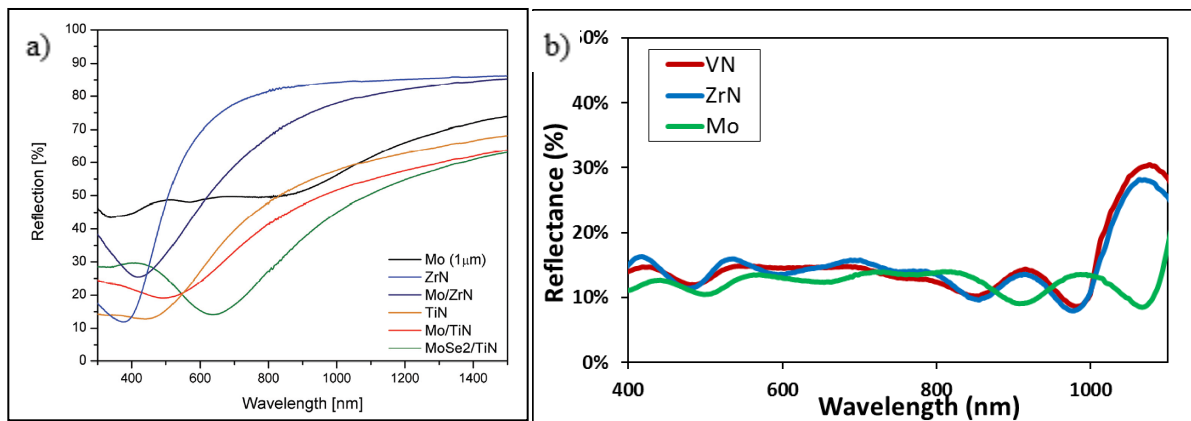

Figure 3.1.1. a) Reflection (to air) for different back contacts, **b)** Reflectance curve for CIGS devices on alternative back contacts.

Multi-layer AR coatings can be used in conjunction with the back reflector to serve as a light trap in the red and the near infra- red region, where enhanced absorption is required. The goal is to achieve at least five passes in the internal reflection for complete absorption of light. The average reflectance of the ultra-thin CIGS devices with alternative back contacts and multi-layer AR coatings (TiO_2/MgF_2/TiO_2/MgF_2) is such that the average reflectance can be considerably reduced, by up to 40%, with this light trapping scheme.

Due to the reduction of thickness of the CIGS layer, there is a decrease in the short circuit current thereby reducing the overall efficiency. As demonstrated, VN and ZrN have higher reflectivity towards the IR and near IR region, thus theoretically increasing the absorption in the region. Figure 3.1.2 compares the QE for CIGS device with the alternative back contact with CIGS device on Mo as back contact. One can see that, in the case of VN, the current indeed increases but that it decreases for ZrN. This demonstrates therefore the capacity of this alternative scheme to produce better current as expected but also shows the limitations of our current process. Another problem arises from the Voc, which tends to be higher for the Mo contact due to better ohmicity.
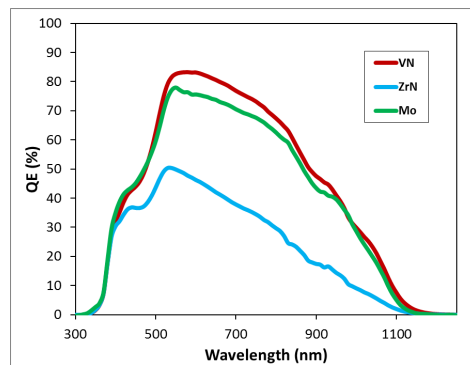

Figure 3.1.2: Quantum efficiency measurements for CIGS devices with alternative back contacts.

Devices with ~ 0.5 µm thick absorber layers were also fabricated on ZrN coated soda-lime glass substrates. The CIGS layer was deposited by a three-stage process. Several differences were adopted for the 0.5 µm CIGS relative to previously optimized CIGS with a standard 2 µm thickness.

- The intended alloy composition was reduced to x ~ 0.15 for 0.5 µm thick CIGS, from x = 0.3 for 2 µm thick CIGS.
- The stage II/III temperature was lowered from 570-620°C which is used for 2 µm CIGS to 540°C for the 0.5 µm CIGS.

Solar cells with 0.5 µm CIGS absorbers were also deposited on the conventional soda-lime glass/Mo substrates for comparison. The device performance results are summarized in Table 3.1.1. The gains in J_{SC} are 1.3 mA/cm^2 and 0.7 mA/cm^2 before and after the deposition of a MgF_2 AR coating. No change in V_{OC} is observed due to the change in the substrate. However, fill factor dropped by ~ 10 % (absolute) due to a decrease in shunt resistance. Further optimization of ZrN deposition conditions as well as surface roughness is required in order to avoid the

degradation in the fill factor due to the decrease in shunt resistance. External QE of solar cells made on ZrN and Mo are shown in Figure 3.1.3. The QE spectrum for ZrN is consistent with the higher reflectance of ZrN in the near infrared region. In future, ZrN should be replaced by HfN, which has an even higher reflectance in this region.

Sample back contact (BC)	d_b (μm)	V_{oc} (V)	FF (%)	J_{sc} (mA/cm^2)	Eff. (%)	R_{series} (Ωcm^2)	R_{shunt} (Ωcm^2)
Standard Mo/CIGS **20564-2-19**	0.55	0.513	62.1	31.1	9.9	3.3	168
Standard Mo/CIGS with AR Coating **20564-2-19**	0.55	0.517	61.7	32.6	10.4	3.4	173
Zr/CIGS Novel BC **20564-1-1 (ZrN)**	0.55	0.514	50.5	32.4	8.4	3.4	82
Zr/CIGS Novel BC with AR Coating **20564-1-1 (ZrN)**	0.55	0.514	50.8	33.3	8.7	3.5	90

Table 3.1.1*: Device performance parameters for CIGS solar cells with ~ 0.5 µm thick absorber layers deposited on both Mo coated and ZrN coated soda-lime glass substrates. Results with and without AR coating are shown.*
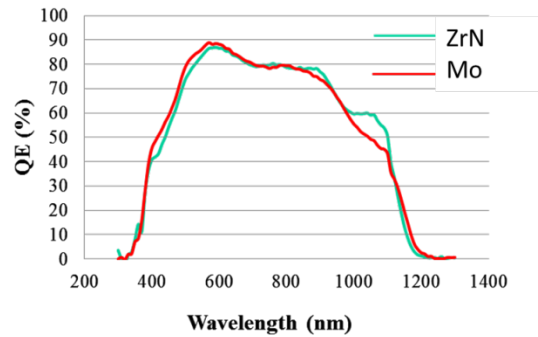

Fig. 3.1.3*. EQE spectra for solar cells deposited on ZrN and Mo coated soda lime glass substrates. The EQE spectrum for ZrN coated substrate is consistent with higher reflectance of ZrN in the near infrared region.*

3.1.2. TCO Back contact
3.1.2.1. Original Structure: SnO$_2$:F/SiO$_2$/SnO$_2$ coated glass substrates
In this task effort, solar cells with standard (2.2 µm) and ultra-thin (0.36 µm) CIGS thicknesses were deposited on SnO$_2$:F/SiO$_2$/SnO$_2$ coated glass substrates without an AR coating and without a back reflector. Optical simulations have shown that TCO's are promising candidates as back contacts that provide light trapping capability for Cu(In$_{1-x}$Ga$_x$)Se$_2$ (CIGS) solar cells. TEC-15, a commercially available glass with a trilayer SnO$_2$:F/SiO$_2$/SnO$_2$ coating (by NSG-Pilkington, Inc.), has been used in this study. The coating structure of TEC-15 is reported to be stable for temperatures to at least 570°C, which is the deposition temperature for CIGS in this study. Although the SnO$_2$:F thickness of TEC-15 is not at the optimum value for maximum J$_{sc}$ in a solar cell having a ultra-thin CIGS layer, the layer is still capable of serving in dual roles both as a contact and as an effective dielectric spacer layer and scattering layer in conjunction with a planar Ag reflector on the back surface of the glass. We are using a back surface Ag layer until a source of nitride back-reflector contacts (to be deposited on the glass first) becomes available. Once nitrides are available, they will be deposited on glass and the SnO$_2$:F will be deposited at

the University of Toledo on the nitride layer to form the back reflector structure. Standard thicknesses were used for all other layers in the solar cell depositions with ultra-thin CIGS reported here. The results are shown in Table 3.1.2 along with the corresponding results for the standard solar cell with a Mo back contact. The highest efficiencies for 2.2 μm and 0.36 μm absorber layers on TEC-15 achieved so far are 6.3 % and 3.3 %, respectively. The TEC-15 coating stack, however, blocks Na from entering into the CIGS. With the incorporation of Na, the efficiency of the 0.36 μm solar cell has been found to increase to 3.7 %.

Sample	d_b (μm)	V_{oc} (V)	FF (%)	J_{sc} (mA/cm^2)	Eff. (%)	R_{series} (W)	R_{shunt} (W)
Reference Mo back contact	2.2	0.63	74	32.1	15.0	2	600
Standard thickness SnO$_2$:F back contact	2.2	0.43	42	34.8	6.3	50	300
Ultrathin CIGS Mo back contact	0.36	0.51	61	24.3	7.5	4	175
Ultrathin CIGS SnO$_2$:F back contact	0.36	0.41	39	20.3	3.3	9	45
Ultrathin CIGS SnO$_2$:F back contact with Na addition	0.36	0.42	40	22.1	3.7	8	45

Table 3.1.2: Performance of CIGS solar cells with Mo and SnO$_2$:F back contacts.

3.1.2.2. Addition of Silver back reflector and alternative TCO

Our approach met challenges due to the low shunt resistance of CIGS solar cells with ultrathin absorbers when deposited onto standard low-cost transparent-conducting-oxide (TCO) coated glass used in the CdTe industry. Even the smoothest TCO coated glass (TEC-15; Pilkington) is quite rough and leads to shunting. As a result, we have been exploring approaches with alternative TCOs.

As an example of the problem, Table 3.1.3 shows the best performance achieved with SnO$_2$:F coated glass (TEC-15). In both cases, Ag reflectors are added to the back of the glass; however, for standard thickness CIGS, this is not expected to generate a significant improvement. For CIGS with a 0.3 μm absorber, the improvement is significant (~0.7%) and the performance is expected to be even higher with the addition of an anti-reflection (AR) coating. It should be noted that we achieved nearly 75% of the performance on 0.3 μm compared to 2.2 μm.

Sample BC = back contact	d_b (μm)	V_{oc} (V)	FF (%)	J_{sc} (mA/cm^2)	Eff. (%)	R_{series} (Ωcm^2)	R_{shunt} (Ωcm^2)
Standard CIGS SnO$_2$:F BC with Ag reflector #20424-3-27 Ag	2.2	0.43	42	34.8	6.3	51	305
Ultrathin CIGS SnO$_2$:F BC with Ag reflector 20481-3 Ag	0.36	0.43	43	25.9	4.7	5	36

Table 3.1.3. Comparison of CIGS solar cells deposited on SnO$_2$:F coated glass (TEC-15, Pilkington),
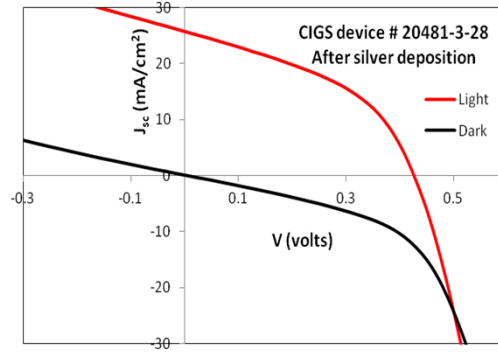
Fig. 3.1.4. Light and dark current-voltage characteristics for a CIGS solar cell with a 0.3 μm absorber layer fabricated on TEC-15 glass substrate (which is coated with a 0.3 μm SnO$_2$:F layer).

Figure 3.1.4 shows the problem with the performance of a cell with a 0.3 μm absorber: a low shunt resistance. It appears from the light and dark J-V characteristics that if the shunt resistance could be increased, a high performance would be possible.

Sample BC = back contact	d_b (μm)	V_{oc} (V)	FF (%)	J_{sc} (mA/cm^2)	Eff. (%)	R_{series} (Ωcm^2)	R_{shunt} (Ωcm^2)
Reference Mo BC	0.36	0.51	60	24.8	7.6	4	131
Ultrathin CIGS SnO$_2$:F BC Stage II/III T=520°C	0.36	0.46	42	21.0	4.0	9	45
CIGS HRT/AZO BC T=540°C	0.35 (nom)	0.277	49.5	30.7	4.21	2	81

Table 3.1.4. Performance of CIGS solar cells with 0.3 μm absorber layers deposited on Mo and on two types of TCO coated glass, including a rough pyrolytic SnO$_2$:F and a much smoother sputtered ZnO:Al. Further efforts are being devoted to improve the performance over that shown in Fig. 3.1.4. Other TCO coated glass substrates have been explored more recently including a sputtered ZnO:Al TCO deposited on SLG. This structure also incorporates a high resistivity transparent layer in an attempt to reduce shunting. Table 3.1.4 shows that this new TCO exhibits increased shunt resistance and thus improved fill factor; however, the voltage has dropped considerably. The net effect is only a slight improvement over the previous best cell with a 0.3 μm absorber.

3.1.2.3. Addition of a MoO$_3$ layer

The possibility of using transparent conducting oxides was explored as an effective component of a back contact/reflector. SnO$_2$:F coated substrates (TEC-15, TEC-7, TEC-8, and TEC-15/HRT from NSG Pilkington), ZnO:Al, and commercial SLG/SiO$_2$/ITO coated substrates were all studied. The results for SnO$_2$:F and ZnO:Al coated substrates have been reported previously. The best results thus far were obtained just recently for SLG/SiO$_2$/ITO substrates. A ~ 10 nm layer of MoO$_3$ was deposited on top of ITO by an ALD process followed by ~ 2-3 nm of NaF by e-beam evaporation. The intended thickness of the CIGS layer was 0.5 μm (Fig. 3.1.5).

The same process modifications were used for this 0.5 μm CIGS layer as was used for the CIGS deposited on ZrN as described above. Solar cell performance results are shown in Table 3.1.5. For comparison, the results on standard Mo substrate are also presented in the table.
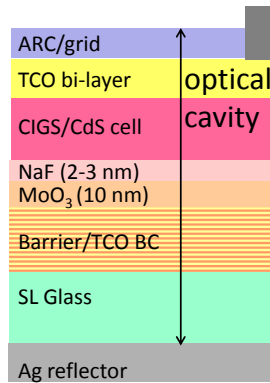
Fig. 3.1.5. *Solar cell structure with ITO back contact, Ag reflector and an AR coating*

	Sample back contact (BC)	d_b (μm)	V_{oc} (V)	FF (%)	J_{sc} (mA/cm^2)	Eff. (%)	R_{series} (Ωcm^2)	R_{shunt} (Ωcm^2)
20564-2.19	Standard Mo/CIGS	0.55	0.513	62.1	31.1	9.91	3.3	168
20564-1.2	SLG/SiO$_2$/ITO/ MoO$_3$ (10 nm)/ NaF/CIGS/ CdS/TCO/grids	0.55	0.521	55.7	26.9	7.81	3.8	155
20564-1.2	SLG/SiO$_2$/ITO/ MoO$_3$ (10 nm)/ NaF/CIGS/ CdS/TCO/grids/ MgF$_2$	0.55	0.522	57.9	27.3	8.26	3.2	166
20564-1.2	Ag/rough-SLG/ SiO$_2$/ITO/ MoO$_3$ (10 nm)/ NaF/CIGS/ CdS/TCO/grids/ MgF$_2$	0.55	0.525	58.8	27.8	8.58	3.1	172

Table 3.1.5: *Device performance parameters of ~ 0.5 μm thick solar cells fabricated on SLG/SiO₂/ITO substrate. Also shown are the parameters for the standard SLG/Mo substrate.*

The solar cell on TCO substrate with a MgF$_2$ AR coating and a Ag layer applied on the backside of glass has an efficiency of 8.5 %. The positive aspect of cell fabrication is that the product FF × V_{OC} for this structure is 30.9 V % which is very close to that for the standard SLG/Mo substrate, which is 31.9 V %. This indicates that the material deposited on TCO has good electronic properties. However, the short circuit current for this structure is lower than that for the standard substrate, which could be attributed to loss of transmission due to modification of the underlying materials of ITO/MoO$_3$ in the CIGS deposition environment.

Thermal stability of the MoO$_3$ films, SLG/SiO$_2$/ITO and SLG/SiO$_2$/ITO/MoO$_3$ substrates were tested by putting the substrates through thermal annealing cycle equivalent to that applied throughout a CIGS fabrication process. Optical transmittance spectra of MoO$_3$-coated SLG substrates before and after thermal annealing did not show any difference. Despite the fact that MoO$_3$ and ITO films exhibited reasonable thermal stability for the intended solar cell application, this does not necessarily mean that such alternative back contact structure is suitable for CIGS solar cells. The MoO$_3$ layer which will be in direct contact with the CIGS layer has to be chemically stable upon deposition of the absorber. In all reported studies of CIGS fabrication on TCO back contacts, including CIGS on MoO$_3$, a thin layer of Ga$_2$O$_3$ has been reported to form at the interface and regarded to the high affinity between Ga and O atoms.

3.1.3. Effect of Sodium

We have studied the distribution of Na in CIGS films deposited for this project and the effect of Na on device performance. In general Na in these devices has a similar effect to those behaviors measured previously. Na has been shown to change preferred orientation toward the low energy close packed (112) planes, which have the fewest interface states and therefore reduce recombination. Na also increases grain size. These are consistent with increased diffusion in the solid, reducing defect density and improving Voc. It is observed that Na enhances reaction of Se with Mo, producing a more ohmic contact at the rear of the device, although this varies among devices.

Because Na has a critical effect on devices it is important to know the distribution throughout the device. In the current devices this also includes the top contacts. Example SIMS analyses of two device layers are shown in Figure 3.1.6. In Figure 3.1.6a selected elements are profiled from a thin ZnO/CdS structure and completely through the device showing uniform Na in the device without significant accumulation at either the front or rear contacts of the structure. In Figure 3.1.6b a profile is given through a finished thin ~7% efficient device. The device has a bilayer conductive/insulating ZnO transparent conductive layer along with a MgF_2 antireflection coating. In the latter figure the signals have been quantified to approximate atomic concentrations where a standard existed. The Ga, In, and Na signals are in arbitrary units. This profile shows a modest accumulation of Na in the CdS layer and some Ga diffusion out of the CIGS relative to the In. Some of these effects may be limited by depth resolution in this profile. However, the addition of ZnO and MgF_2 has only modified the Na profile slightly in this film. Profiling through the CIGS layer in the device showed no variation in the Na throughout the device film, consistent with the profile in Figure 3.1.6a.
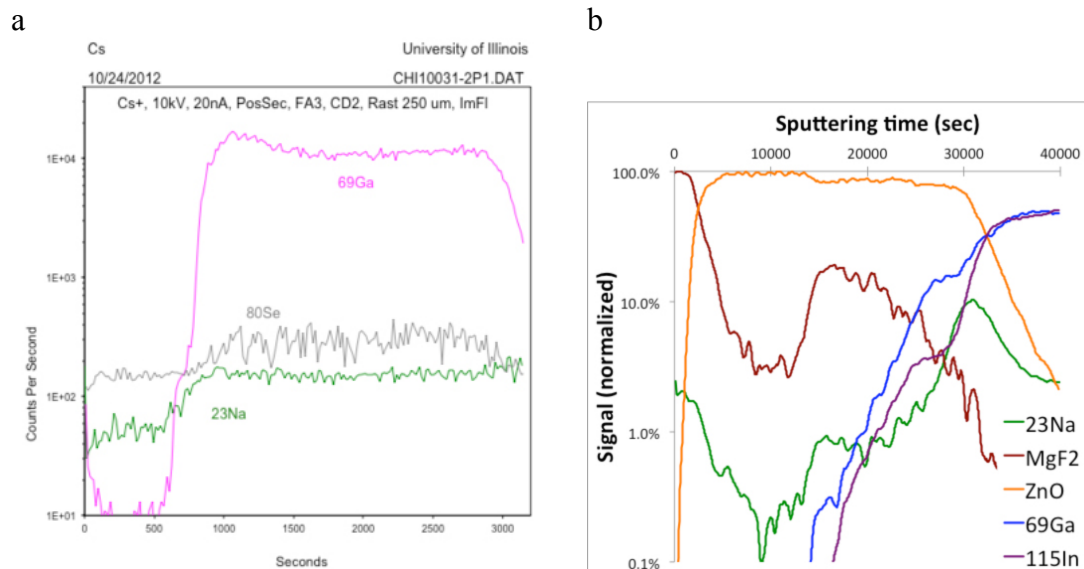
a

b

Figure 3.1.6: SIMS results (a) showing the composition depth profile for layer 10031 coated with ZnO and CdS without accumulation of Na at the heterojunction and (b) a profile of a thin device based on film 10023 was produced. Some Na accumulation at the heterojunction was observed in this finished device. The Na profile is constant in this device throughout the CIGS layer (not shown).

3.2. Task #2 and Task #7 – *Thickness*

Results on these Tasks were reported in the following RPPR-2 reports

- **Report 1**: Use RTSE as the main tool to evaluate the growth process
- **Report 2**: Use RTSE with the 3-stage deposition process
- **Report 3**: Successfully fabricated 0.6 mm CIGS solar cell with 12.1% efficiency (without AR coating). This is comparable with the best ultra-thin CIGS solar cells ever reported by NREL, but from a much lower baseline efficiency (16% vs 18.7%). Successfully developed new procedure for in situ control of the deposition process using real time spectroscopic ellipsometry, specifically for 3-stage deposition process. Successfully developed modeling and procedure for large area mapping of all the layers of the CIGS solar cells via spectroscopic ellipsometry. We have correlated these results with solar cell device performance using a combinatorial approach for optimization.
- **Report 4**: enhance understanding of RTSE for the Stage 1 and stage 2, as well as for large scale mapping. We also deposit ultra-thin CIGS solar cell
- **Report 5**: study the effect of selenium on ultra-thin films and to enhance our understanding of the growth via RTSE
- **Report 7**: enhance understanding of the effect of back contact process on ultra-thin device efficiency
- **Report 8**: detect traps at the nano-scale in CIGS
- **Report 9**: deposit ultra-thin CIGS in both substrate and superstrate configuration with alternative back contact

A summary of the main results can be found below

3.2.1. Baseline: Fabrication of CIGS solar cells by 1-stage process with various thicknesses for the absorber

The purpose of this task was to establish a baseline for our deposition process for various thicknesses of the absorber. We therefore deposited CIGS by co-evaporation using a 1-stage process. The substrate temperature was maintained at 550°C while the targeted composition was a ratio of Cu/(In+Ga)=0.85 and ratio of Ga/(Ga+In)=0.25. The thickness range targeted was from 2.0 mm down to 0.5 mm. All the films tend to be (112) oriented while the FWHM did not show any specific trend even for the thinner films. This is confirmed by cross sectional SEM figures, where the grain size seems to be quite large for all films whatever their thickness. Transmission and Reflection measurements correlate well with composition measurements, with a lower band gap for the 1.55 and 1.30 mm films, while one can observe above band gap transmission as expected for the thinner films (below 1 mm).

CIGS solar cells were then fabricated for the 5 different thicknesses with the following standard structure: glass/Mo/CIGS/CdS/ZnO/ITO/grid. Cells with total area of 0.50 cm^2 were defined by mechanical scribing. The efficiency of the completed device was extracted from J-V measurements under 100 mW/cm^2, and the currents confirmed by QE measurements under white light bias. Results for the devices are reported Table 3.2.1 and Figure 3.2.1. The efficiencies were overall lower than our normal baseline for 1-step process which is around 12-13%, due to a lower current and fill factor than usual. Overall, the trend is the one observed previously, with the current and voltage remaining roughly constant from 2 mm down to 1.3 mm, and decreasing for 0.75 mm and 0.5 mm. One can observe shunts for the cells even with the thickest CIGS film,

which is certainly an indicator of a problem. Also, one can see voltage dependent current collection starting at 1.3 mm, which is unusual.

Even though the efficiencies were lower than anticipated, this is still the first step towards establishing our baseline for thickness dependence. Interestingly, the device with 0.75 mm CIGS had a relatively good efficiency thanks to its good diode behavior and fill factor.

Thickness (μm)	Voc (V)	Jsc (mA/cm^2)	Jsc from QE (mA/cm^2)	Fill Factor (%)	Efficiency (%)
1.95	0.52	28.8	28.5	61.3	9.2
1.55	0.55	27.6	28.5	66.0	10.1
1.30	0.52	28.9	28.6	68.5	10.3
0.75	0.50	25.4	25.0	70.0	8.9
0.50	0.44	22.5	21.0	56.6	5.6

Table 3.2.1: Solar cells parameters for the 5 CIGS solar cells fabricated with the 1-stage process

Figure 3.2.1: J-V and QE results for CIGS cells deposited by a 1-stage process

3.2.2. Study of all 3 stage of the 3-stage process by RTSE

In the scale-up of solar cell processing with thin CIGS for large area photovoltaics (PV) technology, the challenge is to achieve optimum values of layer thicknesses as well as CIGS Cu stoichiometry and alloy composition *x* within narrow ranges and simultaneously over large areas. As a result, contactless metrologies -- those that provide such information in real time are of great interest in this technology, especially in the development of ultra-thin CIGS. We have demonstrated the use of RTSE for real time monitoring and control of thin film CIGS deposition. RTSE has been successfully applied for monitoring the Cu poor to Cu rich and Cu rich to Cu poor transitions during the growth of CIGS films, as described in previous reports. The conventional method of tracking the change in emissivity of the sample may not be sufficiently sensitive for ultrathin films on non-standard substrates. The new methodology developed is

applicable for thicker CIGS films as well. In this report, we describe (i) the use of RTSE for analysis of $(In_{1-x}Ga_x)_2Se_3$ (IGS) during stage I of the deposition process, and (ii) the conversion of IGS into CIGS during stage II and the rapid development of bulk $Cu_{2-x}Se$ during the end of stage II.

3.2.2.1. Stage 1

The RTSE data for the growing IGS samples were analyzed using the three layer model shown in Figure 3.2.2. The layers consist of (i) a Mo/IGS interface roughness layer, having a fixed thickness assumed equal to the roughness layer thickness determined for the Mo surface, (ii) an IGS bulk layer of thickness d_b, and (iii) an IGS surface roughness layer of thickness d_s, the latter two determined individually at each time point in the analysis. Considering (i) and (iii), the Bruggeman effective medium approximation (EMA) was applied to extract the real and imaginary parts of the complex dielectric function for the roughness layers, given by $\varepsilon = \varepsilon_1 + i\varepsilon_2$. A multi-time analysis approach was used in this study to generate a smooth ε for IGS using B-spline functions. These dielectric functions were then parameterized using critical point (CP) and Tauc-Lorentz (TL) oscillators representing the bandgap and the higher energy regions, respectively. This parameterization provides information that can be interpreted in terms of compositional variations and grain size. The resulting dielectric functions are shown in Figure 3.2.3.

Figure 3.2.4 shows the evolution of stage I IGS with $x = 0.31$ obtained by RTSE. The ~ 50 vol.% voids of the ~ 76 Å thick roughness layer on the underlying Mo are filled in by IGS, leading to a rapid increase in the IGS vol.% in the layer from t = 0. Simultaneously, the surface roughness thickness d_s on the IGS increases from $d_s = 0$ as the Mo is covered by IGS. After the interface composition is stabilized, a bulk layer can be incorporated into the model. During initial bulk layer growth, the roughness thickness on the IGS decreases indicating suppression of substrate-induced roughness and apparent wetting of the Mo surface. Later, the IGS roughness increases due to enlarging crystallites protruding above the surface. In addition to the evolution of the structure, the IGS dielectric function and its best fit CP and T-L parameters can be obtained, providing both compositional and grain size fingerprints.
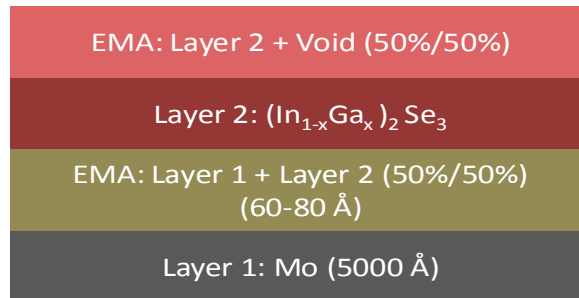

Fig. 3.2.2: Multilayer model used for the analysis of RTSE data acquired on IGS thin films prepared in the first stage of CIGS co-evaporation.
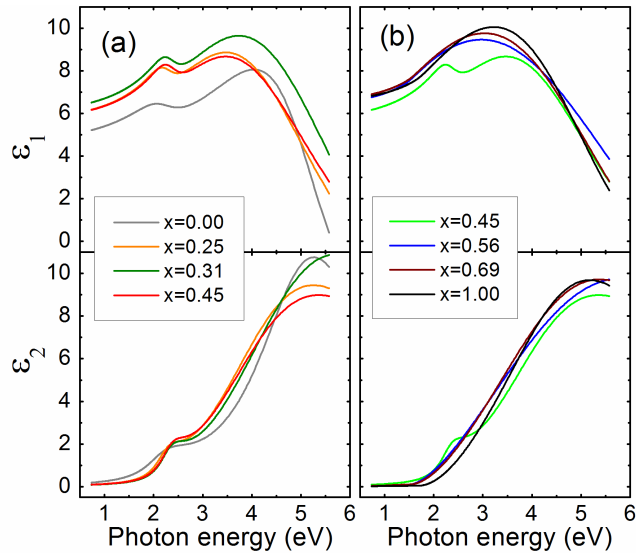
Fig. 3.2.3: Parameterized dielectric functions of IGS films measured at 400°C for (a) $x \leq 0.45$ and (b) $x \geq 0.45$.
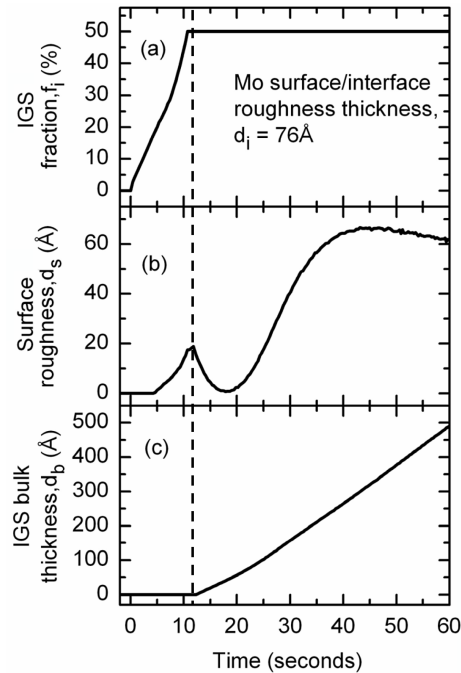

Fig. 3.2.4: Early stage structural evolution of $(In_{1-x}Ga_x)_2Se_3$ (IGS) on Mo coated soda lime glass

The intermediate stage surface roughness evolution, i.e. over the range from 1000 to 2000 Å, is presented in Fig. 3.2.5(a) for selected samples. The results for all samples including the later stage of growth are shown in Fig. 3.2.5(b). The latter figure shows different behaviors for alloyed films with $x \sim 0.2$-0.4 and those with lower and higher x. In fact, the films with $x = 0.25$ and 0.31 are the only ones that show continued roughening throughout the growth process -- all other films show stabilized or smoothening surfaces at the end of deposition. For $x = 0.25$ and 0.31, continuous roughening suggests continuous crystallite growth which generates growing protrusions at the surface, whereas for lower and higher x, smoothening effects are observed,

ultimately (in the limit of thick IGS) yielding flatter surfaces characteristic of the stabilization of a finer grained structure. Figure 3.2.6 shows the monotonic trend in roughness layer thickness at the end of deposition -- near the bulk layer thickness of 9000 Å. The surface roughness thickness shows a rapid decrease when the x value increases above $x \sim 0.31$, which is likely to suggest a rapid reduction in the grain size, leading to smaller, stable protrusions above the surface.
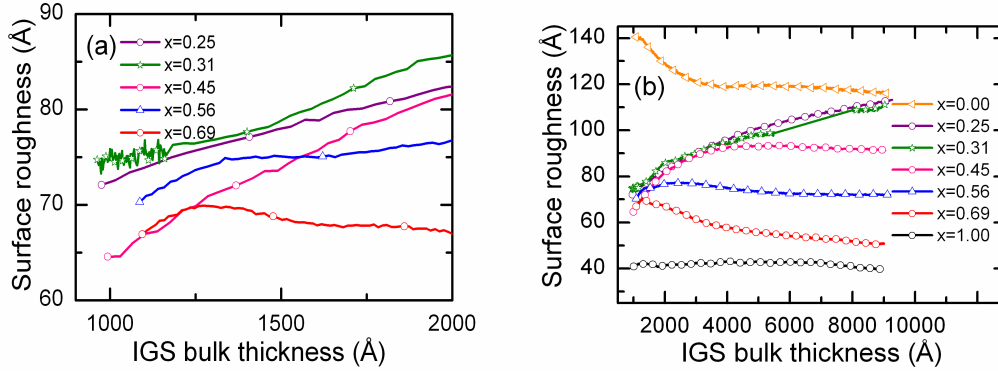

Fig 3.2.5: (a) Surface roughness evolution for IGS films of selected Ga composition x over the bulk layer thickness range of 1000 - 2000 Å; (b) expansion of the results of (a) to the full sample set and a wider bulk layer thickness range.

Fig 3.2.6: Variation of surface roughness with Ga content x at the bulk layer thickness (d_b) of $\sim$ 9000 Å.

The variations of the band gap, amplitude, and broadening of the bandgap critical point oscillator versus alloy composition shows that the In- and Ga- rich sides of IGS have different properties. For $x < 0.5$, the band gap critical point is clearly visible at $E = 2.15 - 2.35$ eV in (ε_1, ε_2) and sharpens with increasing x up to $x = 0.3$. In contrast, for $x > 0.5$, the amplitude of this critical point drops to low values, indicating a suppression of the fundamental band gap structure. In its place, a very broad low energy absorption tail is observed that can be simulated with the onset of the Tauc-Lorentz oscillator.

These results are consistent with previous findings that IGS with $x < 0.5$ has hexagonal crystal structure whereas for $x > 0.6$, it has a disordered zincblende structure. Scanning electron micrographs (SEMs) of the same set of IGS films as was measured by RTSE reveal trends that support the structural and optical behavior from RTSE. First, a strong reduction in grain size is observed between $x=0.31$ and $x=0.54$, which is consistent with the reduction in surface roughness in Figs. 3.2.5 and 6. In addition, the finer grain structure of $x = 0$ relative to $x = 0.31$ is

reflected in the stabilization of the roughness in Fig. 3.2.5(b) for $x = 0$, as compared to a continuous roughening effect consistent with continuing growth of large grains for $x = 0.31$.

3.2.2.2. Stage 2

In this initial analysis of stage II RTSE data, two different models were considered. The first model is a bulk conversion model, in which the entire IGS layer is converted into CIGS uniformly throughout its thickness via an increase in CIGS volume fraction at the expense of IGS (see Fig. 3.2.7). This is in constrast to a layer-by-layer conversion of IGS to CIGS starting from the IGS surface, to be described below (see Fig. 3.2.8). In the bulk conversion model, CIGS nucleates uniformly with depth within the bulk IGS layer, and the grain size and the concentration of grains increase with time at the expense of the surrounding IGS material until the entire IGS layer is consumed. In this process, the bulk layer thickness increases as the Cu is incorporated. Thus, it is assumed that IGS, CIGS and $Cu_{2-x}Se$ components of the bulk layer are resolvable at any time during Cu exposure, and as a result the film is modeled with a uniform bulk layer according to a three-component Bruggeman EMA.
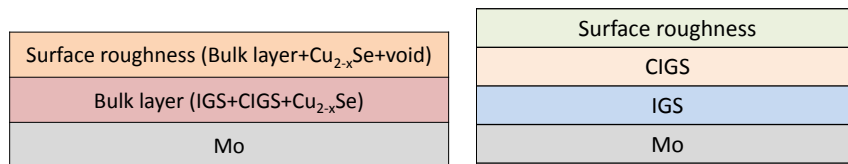
Surface roughness (Bulk layer+Cu_{2-x}Se+void)
Bulk layer (IGS+CIGS+Cu_{2-x}Se)
Mo

Surface roughness
CIGS
IGS
Mo

Fig. 3.2.7: Bulk conversion model for the analysis of stage II RTSE data.
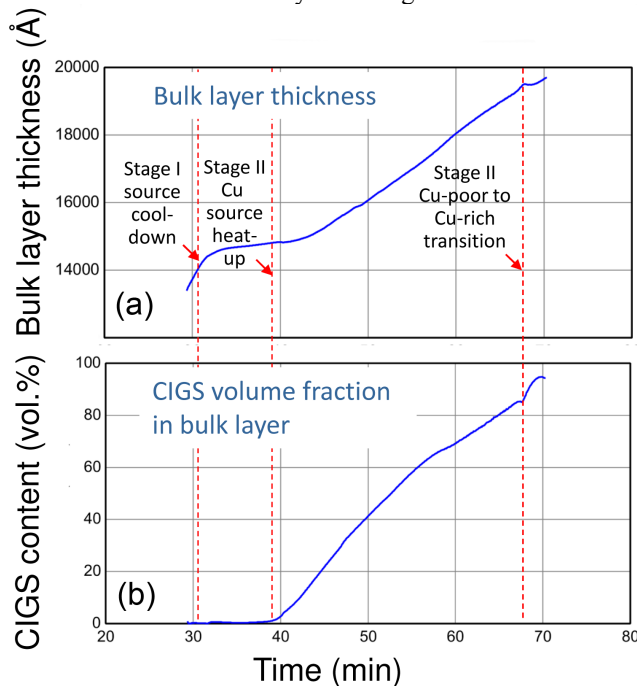**Fig. 3.2.8**: Layer-by-layer conversion model for the analysis of stage II RTSE data.

Fig. 3.2.9: Evolution of (a) bulk thickness and (b) CIGS volume % during stage II obtained on the basis of the bulk conversion model.
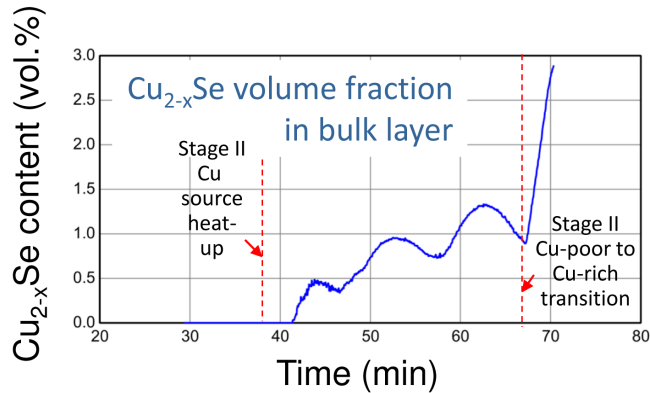
Fig. 3.2.10: A plot of $Cu_{2-x}Se$ content in vol.% within the bulk layer vs. time based on the bulk conversion model.

The second model assumes layer-by-layer conversion in which the top of the IGS layer is converted into CIGS first. The CIGS/IGS growth front then moves downward from the top of the IGS film to the bottom until the entire bulk IGS is consumed and converted into a thicker layer of CIGS. This alternative model is shown in Fig. 3.2.8.

Fig. 3.2.9(a) shows bulk thickness evolution at the end of stage I and throughout stage II, obtained on the basis of the bulk conversion model. The plot shows that there is a rapid increase in IGS thickness during stage I. The growth stops due to the cool down of In and Se sources at the beginning of stage II. When the evaporation of Cu starts, the bulk thickness starts to grow again due to the conversion of IGS into CIGS. In the bulk conversion model, the process starts as small inclusions of CIGS in IGS and the volume fraction of CIGS then increases with time until all the IGS material is converted into CIGS. A plot of CIGS content vs. time is shown in Fig. 3.2.9(b). The initial analysis of stage II shows the presence of some $Cu_{2-x}Se$ even during the Cu poor part of stage II. Fig. 3.2.10 shows a plot of $Cu_{2-x}Se$ content vs. time derived from the bulk conversion model. This is consistent with X-ray diffraction results found in the literature, which suggest some traces of $Cu_{2-x}Se$ as a secondary phase even in Cu-poor CIGS. The rapid increase in $Cu_{2-x}Se$ content towards the end is due to the Cu-poor to Cu-rich transition.

Fig. 3.2.11 shows a plot of IGS and CIGS thickness versus time obtained on the basis of the layer-by-layer conversion model. With this model, however, the IGS thickness did not approach zero at the Cu poor to Cu rich transition; instead, this thickness saturated to ~ 2500 Å. This indicates the lack of sensitivity in detecting a deep CIGS/IGS interface with this model.
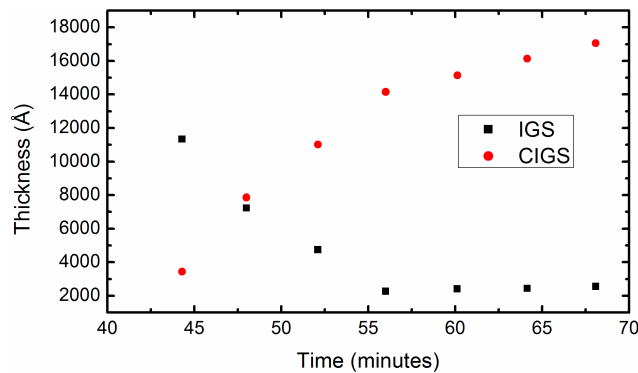

Fig. 3.2.11: A plot of IGS and CIGS thicknesses vs. time based on the layer-by-layer conversion model.

3.2.2.3. Analysis of all Three-Stages of CIGS co-Evaporation by RTSE

A summary of RTSE analysis for all three stages of CIGS growth is presented here, including new results for IGS-CIGS conversion in stage II. The optical models used for the analysis are shown in Fig. 3.2.12. The optical model for stage I analysis incorporates simply IGS bulk and surface roughness layers, whereas the model for stages II and III adds CIGS to the bulk layer and $Cu_{2-x}Se$ to the surface layer.

Figure 3.2.13 shows the bulk layer thickness evolution throughout the three-stage CIGS process. Well-defined average thickness rates can be obtained in three steady state regions of deposition: (i) in stage I throughout IGS bulk layer deposition; (II) in stage II after Cu source stabilization and before saturation of the IGS-CIGS conversion process (see inset of Fig. 13); (iii) in stage III after conversion of $Cu_{2-x}Se$ and during Cu-poor CIGS fabrication. These average rates can be used to evaluate the run-to-run reproducibilities of the total incorporation rates of In+Ga in stages I and III and Cu in stage II.
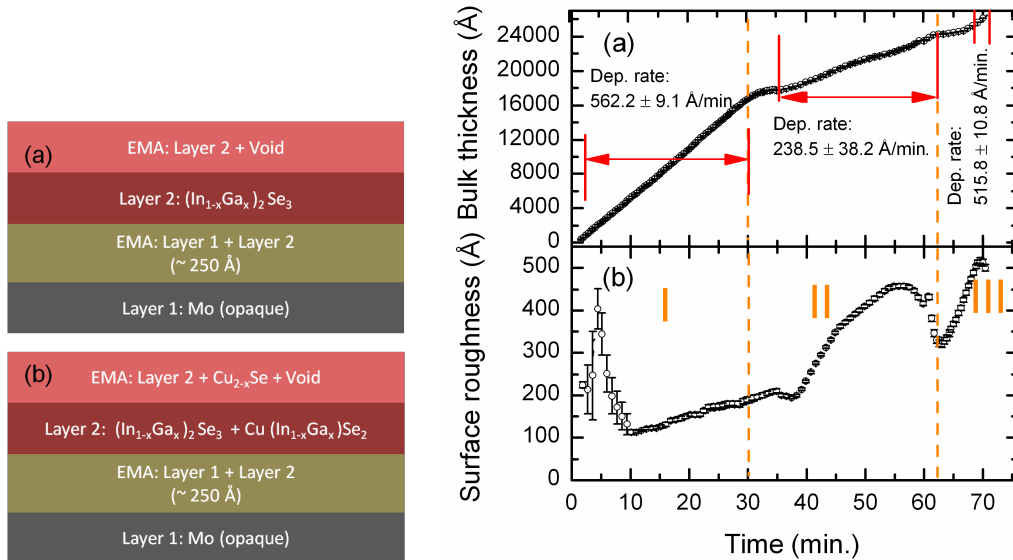

Fig. 3.2.12. Optical modeling schematic for analysis of RTSE data for (a) stage I IGS deposition and (b) stages II and III IGS-CIGS conversion, $Cu_{2-x}Se$ formation, and $Cu_{2-x}Se$-CIGS conversion.

Fig. 3.2.13. (a) Bulk and (b) surface roughness layer thicknesses evolution throughout the three stages of CIGS growth.

In addition to these average rates, the instantaneous rates can be tracked, giving insights into process changes as they occur. In order to separate and characterize the individual In and Ga incorporation rates, the film compositions are needed after the various stages. These can be obtained from the dielectric functions at the end of stage I, and at the Cu-poor to Cu-rich and Cu-rich to Cu-poor transitions near the end of stages II and III, respectively, assuming appropriate databases are available. In fact, database development is in progress. An energy dispersive x-ray spectroscopy (EDS) measurement of the CIGS layer, performed ex situ after deposition, yielded x = [Ga]/{[In]+[Ga]} = 0.25 and y = [Cu]/{[In]+[Ga]} = 0.82. Figure 3.2.13(b) shows the surface roughness layer thickness evolution throughout the three-stage process. In general, roughening is an indication of grain growth processes in which crystallites grow above the film surface plane, whereas smoothening is an indication of coalescence processes.
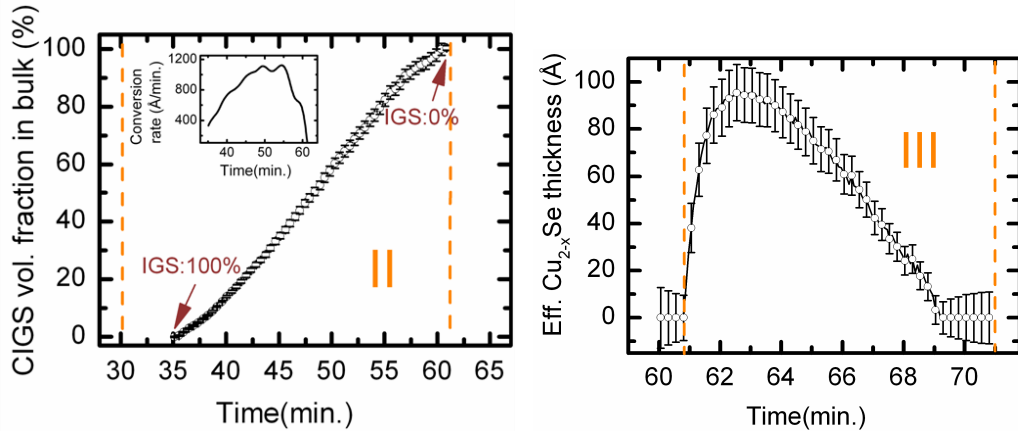
Fig. 3.2.14. Conversion of IGS to CIGS during stage II growth of CIGS. The IGS-to-CIGS conversion rate is shown in the inset.

Fig. 3.2.15. Effective Cu$_{2-x}$Se thickness formed at the surface near the end of the second stage and throughout the third stage. The effective thickness is the volume of Cu$_{2-x}$Se material per unit area of substrate, or the surface layer thickness times the Cu$_{2-x}$Se volume fraction.

Figure 3.2.13 shows that grain growth and coalescence occur in each of the three stages. Most notably, rapid grain growth processes occur as IGS is converted to CIGS and as Cu$_{2-x}$Se is converted to CIGS. Such phase conversions are characterized in Figs. 3.2.14 and 15, where the evolution of the CIGS component in the bulk layer and the Cu$_{2-x}$Se component in the surface layer are depicted, respectively, during stage II. After all IGS is converted to CIGS as shown in Fig. 3.2.14 near the end of stage II, the Cu$_{2-x}$Se phase rapidly develops as shown in Fig 3.2.15. Again, the magnitude of the observed roughening processes, as well as the phase conversions, can be used to evaluate reproducibility of three-stage growth and in correlation with solar cell performance. The highest efficiency 0.5 cm^2 CIGS cell from this deposition was ~ 13%.

3.2.3. SE mapping and correlation with device performance

Results and Discussion

Figures 3.2.16(a) and (b) show maps, spanning the 10 cm × 10 cm area of the Mo/SLG substrate, for the CIGS bulk and surface roughness layer thicknesses, the latter extracted using the Bruggeman effective medium approximation. The maps show well-defined circular patterns with bulk and roughness layer thicknesses in the ranges of 6000-7600 Å and 265-370 Å, respectively, yielding a CIGS effective thickness from 6160 Å to 7820 Å. The effective thickness is the volume per unit substrate area and is the sum of contributions from the bulk, surface, and interface roughness layers. Figures 3.2.16(c) and (d) show maps for CdS deposited in the CBD process. The effective thickness of the CdS layer is in the range of 420-660 Å and, in contrast to the CIGS layer, is thinner at the substrate center. The large CdS roughness (for such a thin layer), which smoothens with increasing CdS bulk thickness, is caused by the surface modulations of the underlying rough CIGS layer.

Figures 3.2.16(e-g) focus on the sputtered transparent conducting oxides of intrinsic ZnO (i-ZnO), which contacts the CdS, and doped ZnO (ZnO:Al), which contacts the i-ZnO. Both layers are relatively uniform with effective thickness ranges of 840-990 Å, excluding the top right edge region, and 2900-3460 Å.

Along with the bulk thickness and surface roughness maps for CIGS, a compositional map was also obtained. The same SE analysis procedure that yielded the maps of Figs. 3.2.16(a-b) also yielded the Ga content map which is shown separately in Fig. 3.2.17. The map shows a circular compositional pattern with the Ga content in the range of ~ 0.2-0.3. The lowest Ga content is near the top of the map and the highest Ga content is towards the bottom, which is consistent with the position of the sources in the evaporation chamber.

Fig. 3.2.16: Solar cell component layer thicknesses obtained using step-by-step mapping SE including: CIGS (a) bulk and (b) surface roughness, CdS (c) bulk and (d) surface roughness, (e) ZnO:Al bulk and (f) surface roughness, and (g) intrinsic ZnO layer thickness.

CIGS d_{eff} (μm)	V_{oc} (V)	FF (%)	J_{sc} (mA/cm^2)	Efficiency (%)
0.731	0.55	70.7	32.7	12.8
0.740	0.55	69.2	32.0	12.1

Table 3.2.2. Performance of thin CIGS solar cells.

The performances of the two highest efficiency cells are shown in Table 3.2.2, and lie within the 12% range for thicknesses of 0.70-0.75 μm. The low efficiencies toward the bottom of the map are clearly due to low fill factor values, which are often associated with the presence of shunts and/or voltage-dependent collection (VDC).

Figure 3.2.18(a) shows the correlation of short circuit current density (J_{sc}) vs. the Ga content (x). The figure reveals a clear decrease in the short circuit current with an increase in the Ga content. This decrease is associated with an increase in the bandgap of the material, which occurs as the Ga content increases. Figure 3.2.18(b) shows the correlation of the efficiency vs. the Ga

content. This plot reveals the same trend as the plot of J_{sc} vs. Ga content because, for solar cells with thin CIGS, the efficiency is dominated by J_{sc}.
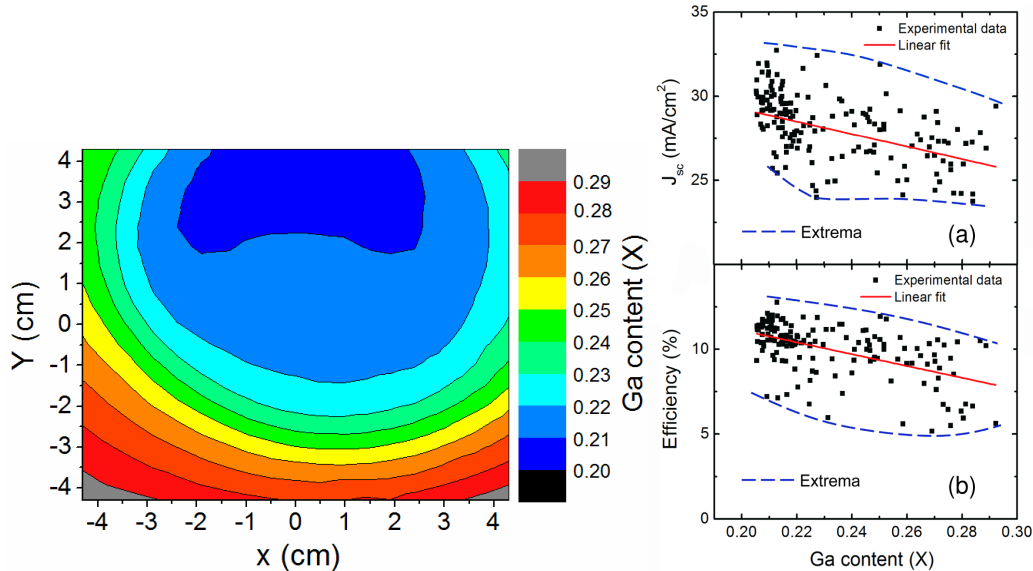

Fig. 3.2.17: Map of the Ga content x over the 10 cm x 10 cm area obtained from SE analysis of CIGS on the Mo coated soda lime glass substrate.

Fig. 3.2.18: (a) Correlation plot of J_{sc} with Ga content x; (b) correlation plot of efficiency with x.

The correlation plot of Fig. 3.2.19(a) shows the expected increase in J_{sc} with CIGS bulk layer thickness. The correlation plot of Fig. 3.2.19(b) shows the decrease in J_{sc} with an increase in the CdS layer thickness. This is consistent with the fact that the absorbed light in the CdS layer does not contribute to J_{sc}. This plot also suggests that the efficiency for a given CIGS thickness may be improved in this study by a reduction in CdS thickness. The correlation plot of J_{sc} vs. ZnO:Al thickness is shown in Fig. 3.2.19(c). The plot shows a very weak negative correlation between the parameters. The dependence of J_{sc} on ZnO:Al thickness is not due to the change in series resistance presented by ZnO:Al, as J_{sc} is independent of series resistance as long as the resistance is low, as is the case here. If the series resistance is too high, however, the voltage drop across this resistance turns on the PV diode even under short circuit conditions. Then J_{sc} depends on the series resistance magnitude, but only in poor low-FF cells. The dependence of J_{sc} on ZnO:Al thickness in the plot is a subtle optical effect, in fact, due to a shift in the position of the fringes apparent in the QE spectrum with the change in ZnO:Al thickness.

In Fig. 3.2.19(d) a correlation plot of V_{oc} vs. CIGS thickness is shown; however, the trend here is not yet understood. The weak negative correlation of V_{oc} with effective CdS thickness evident in Fig. 3.2.19(e) can be explained by the fact that V_{oc} has a logarithmic dependence on J_{sc}. Thus, a thicker CdS layer decreases not only J_{sc}, but also V_{oc}. The presence of shunt and series resistances in the solar cells can be reflected in Fig. 3.2.19(f) and Fig. 3.2.19(g), which are the plots of fill factor vs. CIGS bulk thickness and effective CdS thickness, respectively. Figure 3.2.19(f) suggests that the fill factor increases with increasing CIGS thickness for solar cells with thin CIGS layers. This can be expected due to an increase in grain size with thickness for thin CIGS, which may lead to a decrease in defect density. The dependence is very weak for these cells, however. Fig. 3.2.19(g) shows that the fill factor decreases with an increase in effective CdS thickness. In Fig. 3.2.19(h), the plot of efficiency vs. CIGS thickness is shown, which

reveals a similar trend as the plot of J_{sc} vs. CIGS thickness, but the data points are more scattered due to other non-idealities present in the solar cells such as shunt and series resistances. 3.2.19ure 4(i) shows the decrease in efficiency with an increase in effective CdS thickness. The data points are again comparatively more scattered for the same reason.

The scatter in all the plots of Fig. 3.2.19 can be attributed in part to the fact that, for the given thickness plotted, other thicknesses are varying that impact device performance; variations in shunt resistance and/or VDC also play a role. As a result, in future work, the mapping approach in conjunction with the composition and thickness non-uniformities of the layer components will provide a combinatorial approach to optimization. This is important since, as the thickness of CIGS is reduced, the materials characteristics of the optimum device are likely to change from those of cells with the standard CIGS thickness, examples being the CIGS composition and the CdS thickness. A combinatorial approach enables optimization of multiple parameters in a single deposition.
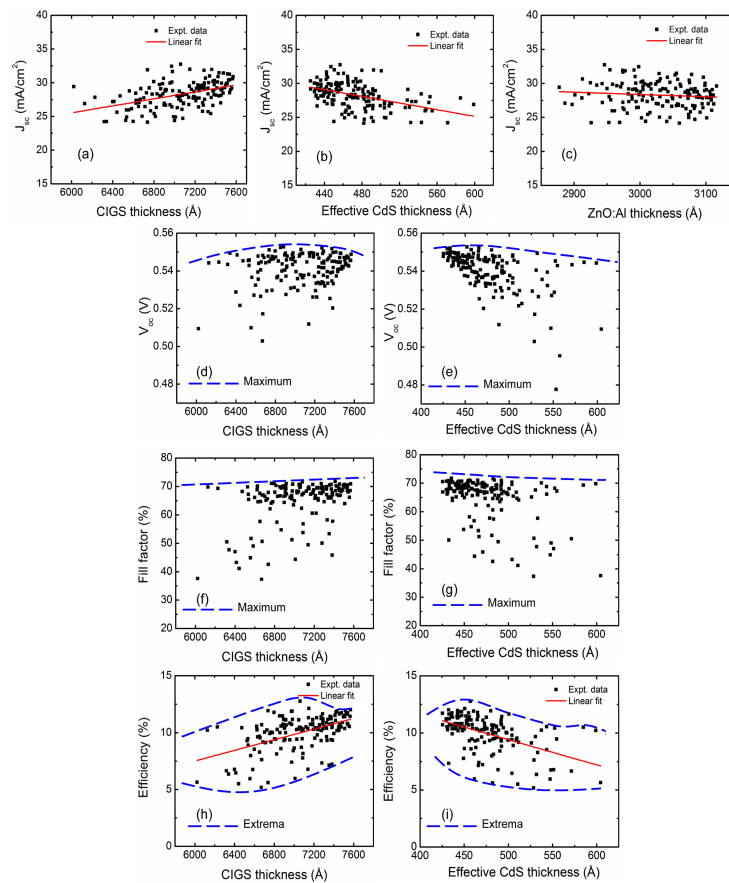

Fig. 3.2.19: Correlation plots of (a) J_{sc} vs. CIGS bulk thickness, (b) J_{sc} vs. effective CdS thickness, (c) J_{sc} vs. ZnO:Al thickness, (d) V_{oc} vs. CIGS bulk thickness, (e) V_{oc} vs. effective CdS thickness, (f) FF vs. CIGS bulk thickness, (g) FF vs. effective CdS thickness, (h) efficiency vs. CIGS bulk thickness, and (i) efficiency vs. effective CdS thickness.

3.2.5. 0.50 micron CIGS with ITO/MoO$_3$ substrate

In this section CIGS solar cells with intended absorber layer thickness of 0.50 μm were fabricated onto SLG/SiO$_2$/ITO/MoO$_3$ substrates and studied. J-V characteristics and QE spectra are presented for the two highest efficiency solar cells obtained from the solar cell deposition; device no. 20584-1-1 and device no. 20584-3-2. The solar cells are fabricated for the purpose of light illumination from the film side, however, cell efficiency and QE spectra were recorded for film side illumination as well as glass side illumination for comparison.

For solar cell no. 20584-3-2, the experimentally measured QE spectra for film side illumination and glass side illumination are compared in Figure 3.2.20 (top), and the corresponding J-V characteristics in the dark and under standard AM 1.5 illumination for film side illumination and glass side illumination are shown in Figure 3.2.20 (middle) and Figure 3.2.20 (bottom), respectively. For film side illumination, the solar cell exhibited the following performance parameters: $V_{OC} = 0.552$ V, $J_{SC} = 28.1$ mA/cm^2, FF = 58.3%, and efficiency $\eta = 9.0\%$. On the other hand, under glass side illumination, the solar cell exhibited the following performance parameters: $V_{OC} = 0.451$ V, $J_{SC} = 9.2$ mA/cm^2, FF = 45.8%, and efficiency $\eta = 1.9\%$.

For these solar cells, efficiency for film side illumination is much higher than that recorded under glass side illumination. That could be regarded to degrade optical transmittance of the MoO$_3$ layer upon deposition of the CIGS layer, or that majority of the incident light is absorbed near the back contact where the absorber is fully or partially inactive for ultra-thin CIGS solar cells on Mo back contact, or a combination of both effects.
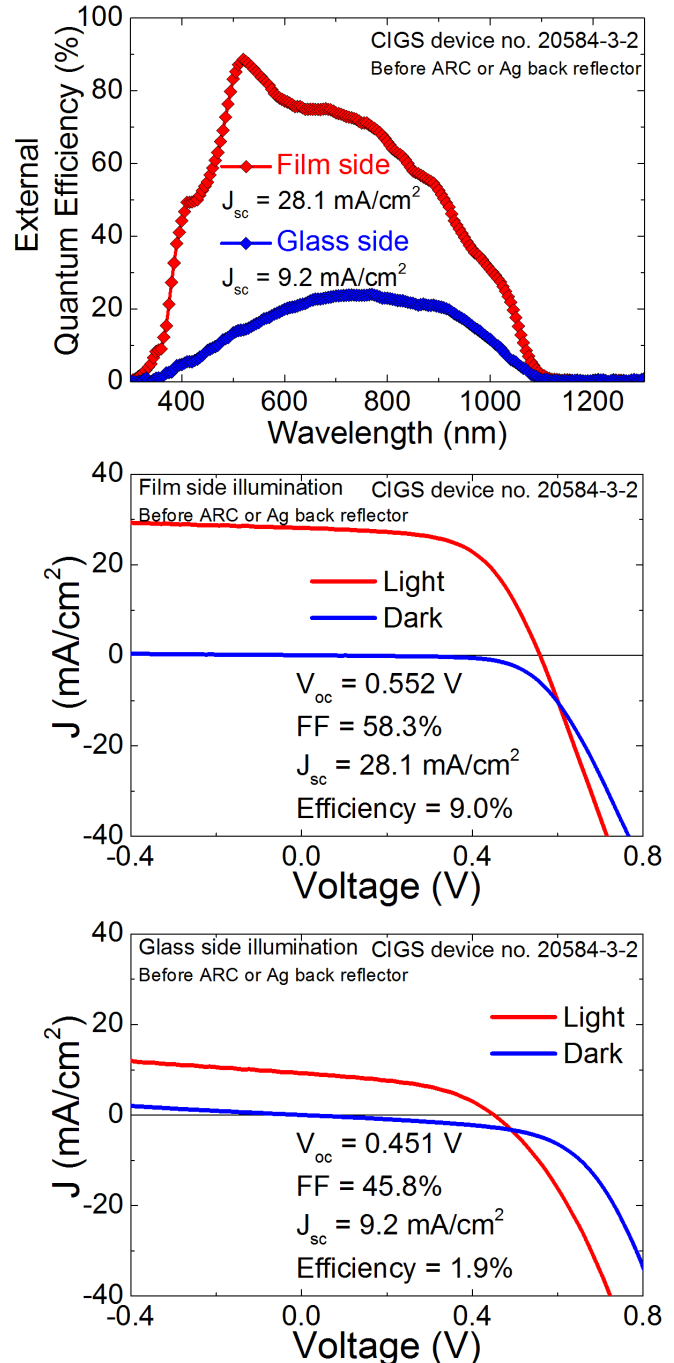
Figure 3.2.20: (Top) comparison of experimentally measured QE spectra for CIGS solar cell no. 20584-3-2 with 0.50 μm absorber layer recorded for film side illumination and glass side illumination; (middle) J-V characteristics of CIGS solar cell no. 20584-3-2 recorded under film side illumination; (bottom) J-V characteristics of CIGS solar cell no. 20584-3-2 recorded under glass side illumination.

3.2.6. Fabrication of high efficiency solar cells with ultra-thin CIGS

With the optimization of our 3-stage deposition process via in situ and real time spectroscopic ellipsometry, we were able to increase the efficiencies of our solar cells with thin CIGS layers having thicknesses of 0.7 μm, 0.5 μm and 0.36 μm. To our knowledge, these are among the highest efficiencies reported for cells with ultra-thin CIGS. The results are summarized in Table 3.2.3.

	Sample back contact (BC)	d_b (μm)	V_{oc} (V)	FF (%)	J_{sc} (mA/cm^2)	Eff. (%)	R_{series} (Ωcm^2)	R_{shunt} (Ωcm^2)
20564-2.19	Standard Mo/CIGS	0.55	0.513	62.1	31.1	9.91	3.3	168
20564-1.2	SLG/SiO$_2$/ITO/ MoO$_3$ (10 nm)/ NaF/CIGS/ CdS/TCO/grids	0.55	0.521	55.7	26.9	7.81	3.8	155
20564-1.2	SLG/SiO$_2$/ITO/ MoO$_3$ (10 nm)/ NaF/CIGS/ CdS/TCO/grids/ MgF$_2$	0.55	0.522	57.9	27.3	8.26	3.2	166
20564-1.2	Ag/rough-SLG/ SiO$_2$/ITO/ MoO$_3$ (10 nm)/ NaF/CIGS/ CdS/TCO/grids/ MgF$_2$	0.55	0.525	58.8	27.8	8.58	3.1	172

Cell #		CIGS d_{eff} (μm)	V_{oc} (V)	FF (%)	J_{sc} (mA/cm^2)		Eff. (%)	
20408-1-5 570°C (II/III) (no AR)	20408-1-5 570°C (II/III) (MgF$_2$ AR)	0.73 (x = 0.22)	0.55	70.8	32.7	33.8	12.8	13.2
20564-2-19 Mo: 250°C CIGS: 550°C (no AR)	20564-2-19 Mo: 250°C CIGS: 550°C (MgF$_2$ AR)	0.55 (x = 0.15)	0.512	61.7	31.1	32.6	9.9	10.4
Mo: 250°C CIGS: 540°C (no AR)	Mo: 250°C CIGS: 550°C (MgF2 AR)	0.35 (x = 0.11)	0.464	65.3	28.5	30.3	8.7	9.1

Table 3.2.3: High efficiency solar cells fabricated for ultra-thin CIGS

3.2.7. Thin CIGS: Direct nm-scale spatial mapping of traps in CIGS

Many traps have been reported in CIGS. Of particular interest are the traps near mid-gap that might serve as efficient generation-recombination centers leading to open circuit voltage reduction. The E_V +0.47 eV trap is a common mid-gap state that has been potentially assigned to In vacancies and but where these defects are located and what role the microstructure has not been established. Using newly developed nanometer-scale deep level transient (nano-DLTS) spectroscopy, the spatial distribution of the E_V+0.47 eV trap in p-type Cu(In,Ga)Se$_2$ (CIGS) is mapped simultaneously with topography to correlate the electrical traps with physical structure. Here using nano-DLTS, the spatial distribution and correlation with microstructure is determined and compared with traditional defect spectroscopy methods to demonstrate the correlation of macro- and nanometer-scales. It is demonstrated that the E_V+0.47 eV trap properties from nano-DLTS match the macroscopic properties. The map of the E_V+0.47 eV reveals that this trap is not uniformly distributed, is likely correlated with specific grain boundaries, and not related to all grain boundaries.

Before characterizing the traps locally, conventional DLTS was performed. Figure 3.2.21 shows the DLTS spectrum with two peaks/traps and Figure 3.2.21 right shows Arrhenius plots for the E_V+0.27 eV and E_V+0.47 eV levels. The average trap concentrations and cross-sections are given in Table 3.2.4. These traps have been characterized in similar CIGS materials and have been attributed to various sources. However, the presence and concentration of these traps are typical of high quality films. With the general material quality assessed, the E_V+0.47 eV was focused on with the nano-DLTS to demonstrate its capabilities and because a trap at E_V+0.47 eV is likely to be an efficient generation-recombination center.
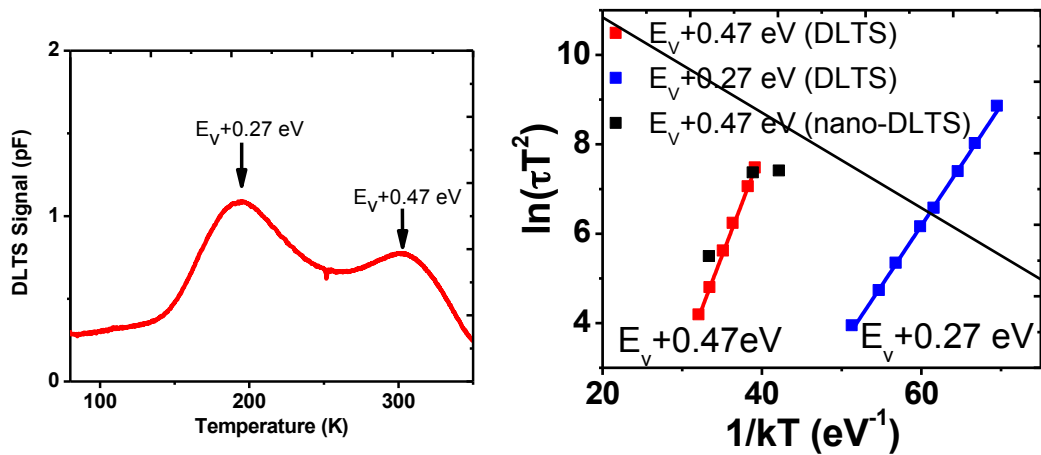

Fig 3.2.21. *DLTS signal of the 80 s^{-1} rate window of CIGS showing traps E_v+ 0.27 eV and E_v+0.47 eV.* ***Right****: Arrhenius plot of DLTS and nano-DLTS measurements. The nano-DLTS Arrhenius data aligns well with the E_V+0.47 eV trap measured by DLTS indicating the nano-DLTS trap measured in this temperature range was the E_V+0.47 eV trap.*

Activation Energy	Cross Section	Concentration
Ev+0.27 eV	1×10^{-17} cm^2	2×10^{14} cm^{-3}
Ev+0.47 eV	2.2×10^{-17} cm^2	9×10^{13} cm^{-3}

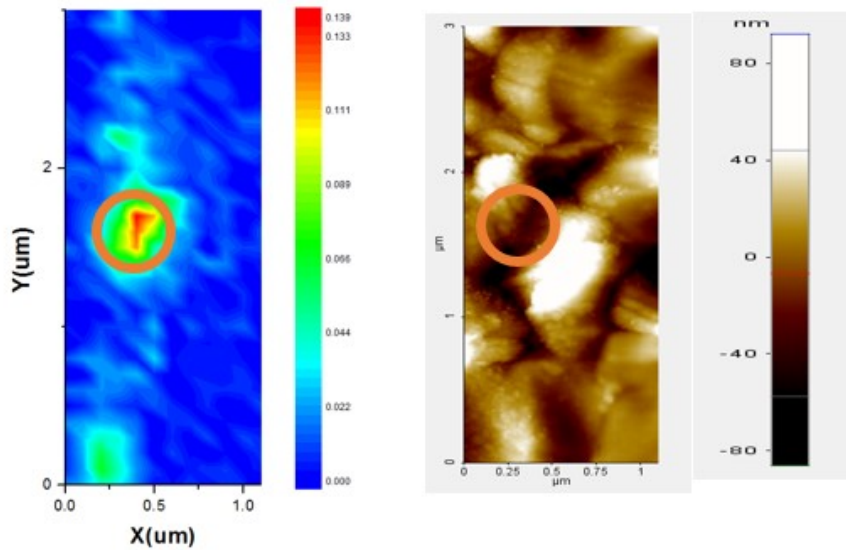Table 3.2.4: SUMMARY TRAP SIGNATURES AND DEEP LEVEL CONCENTRATION IN CIGS FILM.

Fig. 3.2.22: SKPM map of the surface potential signal showing large signal likely in small grain region. The black line corresponds to the approximate edge of the schottky metal. The signal is only obtain in the bare CIGS depletion region. (Left) Topography image of the same area. (Right)

In the mapping mode, the surface potential (SP) transient is recorded at each position. If the total change in SP from t = 0 to t = ∞ (ΔSP_0) is mapped for each location, it reveals a map of all traps because they all respond in this time frame. Therefore to map individual trap levels, it is necessary to measure the SP change over smaller windows of time. Indeed, the same double boxcar approach used in DLTS and isothermal double boxcar analysis can be used for nano-DLTS mapping. Here, the change in SP (ΔSP), defined as $\Delta SP(t_1, t_2) = SP(t_2) - SP(t_1)$, where t_2 and t_1 are times ($t_2 > t_1$), is mapped. Thus t_1 and t_2 define the leading and trailing edges of the effective rate window. Any traps the fully emit before t_1 or after t_2 will not be detected, providing for selection of specific traps based upon their unique temporal behavior. Figure 3.2.22 shows a nano-DLTS map at 298 K where the E_V+0.47 eV trap time constant was ~16 ms, the ΔSP times were chosen to be 7.7 ms and 30.8 ms to maximize sensitivity to the E_V+-0.47 eV trap. At this temperature, the E_V+0.27 eV trap time constant is ~20 μs and has completely emitted before the ΔSP times indicating no contribution of this level to the map. First, to verify the observed map corresponded to the E_V+0.47 eV level, transients were recorded at the peak (red) spot at different temperatures and compared with the DLTS results.
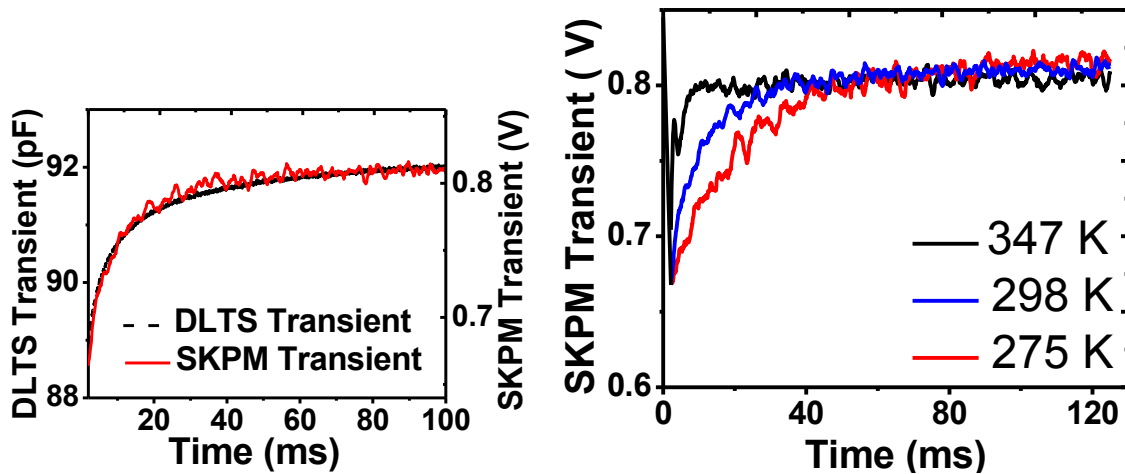
Fig. 3.2.23: DLTS transient and SKPM relative surface potential transient are plotted using same time scale. Right: SKPM transient at 275K, 298K and 347 K are plotted. SKPM transient time constant is decreasing with temperature.

Figure. 3.2.23 shows the DLTS and nano-DLTS transients at 298 K where the transient shape are nearly identical. At different temperatures, the nano-DLTS transients in Fig. 3.2.23 right show temperature dependence indicative of trapping effects and plotting the extracted time constants with the DLTS Arrhenius data in Fig. 3.2.21 shows good agreement indicating the nano-DLTS is tracking only the $E_V+0.47$ eV level under these conditions. The map in Fig. 3.2.22 shows multiple regions of $E_V+0.47$ eV trapping with the largest peak exhibiting a ~0.14 V transient magnitude, which currently we estimate to correspond to a ~10^{15} cm^{-3} local trap density. This map has been repeated for many different regions and in every case, the $E_V+0.47$ eV trap is found in valley areas likely at particular grain boundaries. However, the trap has never been detected inside the grains and is not located at ever grain boundary indicating either the importance of grain boundary angle or preferential impurity segregation/intrinsic defect formation at particular grain boundaries.

The $E_V+0.47$ eV trap has been attributed to In vacancies or Fe impurities. Here we cannot confirm these attributions, but both Rincon et al. and Zhang et al. have indicated in similar CuInSe$_2$ material that V_{In} defects could form levels at 0.17-0.25 eV and 0.41 eV. If we determine the $E_V+0.27$ and $E_V+0.47$ eV levels are collocated, it would give credence to the V_{In} attribution. Additionally, nm-scale chemical and structural techniques to determine the exact mechanism at play within these regions is underway. So far, the $E_V+0.47$ eV level has be correlated with physical structure (i.e. likely grain boundaries) and any links to its chemical nature is underway.

3.3. Task #3 and Task #8 – *CBD and CdS free buffer layer*

Results on these Tasks were reported in the following RPPR-2 reports

- **Report 1**: deposit a ZnS based compound by ALD and characterize its properties.
- **Report 2**: Compare ZnS based compound by ALD with layers deposited by CBD.
- **Report 3**: Successfully deposited ZnS by ALD on a 0.8 mm CIGS device and demonstrated enhanced current generation. Successfully deposited and studied ZnS and InS compounds and characterized them for solar cell application. Developed an optical model to include the effect of the buffer layer on the device efficiency

A summary of the main results can be found below

3.3.1. ZnS deposited by CBD

The thin films of ZnS were deposited onto a 1.99 nm native oxide coated Si(100) substrate using chemical bath deposition. Two solutions were prepared for the purpose of this deposition. Solution 1, a mixture of 29.78g $ZnSO_4.7H_2O$ and 250 ml 18.2 kΩ de-ionized water, and Solution 2, consisting of 31.54g Thiourea and 250 ml de-ionized water.

The solutions were left to stir for 30 minutes at a temperature setting of 50°C using a hot plate and a magnetic stirrer. The solutions were poured into precise dispensers and kept ready for the deposition. The deposition beaker is filled with 80 ml of Solution 1 and kept in the water bath until temperature reaches 75°C. Afterwards, 80 ml of Solution 2 is gently poured while being stirred in through the course of 10 seconds to allow the formation of Zinc sulfate and Thiourea complexes. The reaction is allowed to occur for 5 minutes, at which 61 ml of Ammonia is stirred in. The addition of Ammonia will create small, white colored precipitation which can be dissolved by stirring, provided that the Ammonia concentration is enough – in our case, the Ammonia usage is in excess due to the constant evaporation from the temperature being close to boiling.

At this point, samples clipped together, consisting of a Si(100) wafer and two microscope slides made of soda lime glass (SLG) are inserted into the solution. The timer is set to 2 hours and 30 minutes and every 5 minutes, the samples are lifted out of the solution and then submerged 10 times to rid the deposition surface from growth inhibiting parasitic deposition.

At the end of the deposition, a visible, undesired sedimentation on the surface is observed, which can be alleviated with a 10% rinse consisting of de-ionized water and Ammonia. This procedure is followed by a second rinsing stage using only de-ionized water. The samples are then dried with ultra high purity (UHP) Nitrogen gas and placed into a dry furnace set to 120°C. This annealing process is timed to a precise 5 minutes, due to the high risk of degradation that may occur in the CIGS layer once the ZnS is formed on the surface of a $CuInGaSe_2$ solar cell.

The CBD-ZnS-Si(100) sample was then analyzed using an *ex-situ* spectroscopic ellipsometer. Data were acquired after film growth using a rotating-compensator multichannel ellipsometer with a photon energy range of 0.75 to 6.5 eV at angles of incidence of 50°, 60° and 70°. Pairs of ((ψ, Δ) spectra were collected with an acquisition time of 3 s. Analyses of the spectra involved numerical inversion and least-squares regression algorithms. The optical model for the film consisted of a bulk layer whose dielectric function is determined in the analysis and a surface roughness layer whose dielectric function is determined from an effective medium theory as a 0.5/0.5 volume fraction mixture of the bulk layer and void.

The ellipsometric parameters (*ψ, Δ*) were measured as a function of energy for various numbers of cycles and angles of incidence. Analysis of these parameters allowed for the extraction of the bulk thickness, d_b, and of the surface roughness, d_s. 2.5 hour chemical bath

deposition yielded a bulk thickness of 79.15 nm with a roughness of 2.269 nm. This bulk layer thickness corresponds to a growth rate of 0.528 nm/minute.

The same ellipsometric parameters (ψ, Δ) used to fit (d_b, d_s) were also used to extract the dielectric functions ($\varepsilon_1, \varepsilon_2$) versus energy, and plot the real (ε_1) and imaginary (ε_2) components of the complex dielectric function as a function of energy for the deposited film. The main distinctive feature of this spectrum is the fundamental interband transition which was fitted with a parabolic band critical point oscillator. This bulk fundamental energy-gap (E_o) at 3.6 eV shows a well-defined excitonic structure and is in good agreement with previous work.

3.3.2. Deposition of ZnS by ALD on a 0.8 um CIGS device

ZnS thin films were deposited on 0.8 μm CIGS solar cell using Atomic Layer Deposition (ALD). Research grade nitrogen gas was used to pulse and purge the precursors from the ALD chamber. Diethyl zinc and Dimethyl sulfide were used as sources for zinc and sulfur, respectively. The pulse time for zinc was 0.3 second and for sulfur 0.1 second. Purge time was 20 seconds for both precursors in order to prevent them from reacting in the gas phase within the chamber. A flow rate of 5 sccm was used with the precursors at room temperature and the chamber heater was set at 120°C.

The J-V results for the solar cells are plotted in Figure 3.3.1 Left, while the QE results are plotted along with the results for a solar cell with CBD-CdS. As one can see, the deposition of a ZnS buffer layer allows generating higher current than a standard CBD-CdS layer (36 mA/cm^2 vs 34 mA/cm^2). The Voc and FF for both buffer layers were similar (0.39 V and 0.38 V, 55.1% and 53.8% for ZnS and CdS respectively), leading to a higher efficiency of 7.7% for the ZnS buffer layer.
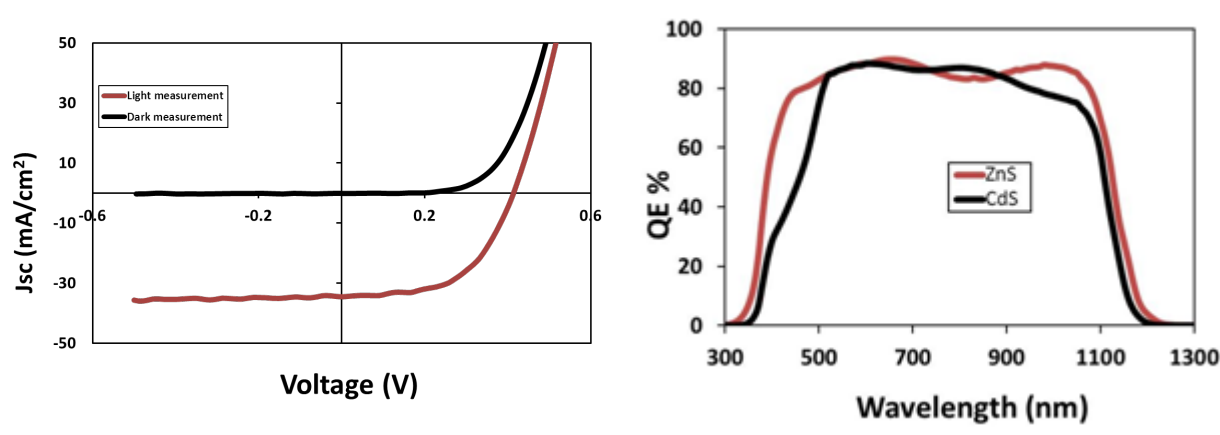

Figure 3.3.1: J-V and QE for CIGS solar cell with ZnS ALD compared to CdS CBD

3.3.3. Deposition of InS by CBD

ZnS and InS compounds were deposited by chemical bath deposition and their optical properties measured by spectroscopic ellipsometry. Their optical constants are reported in Figure 3.3.2, along with the ones from CBD CdS. As expected, CdS has the smallest band gap while ZnS and InS have relatively similar values. It is interesting to note that InS does not have the same sharp transition as ZnS, which has been observed previously. QE was measured on an ultra-thin CIGS solar cell with CBD CdS, and QE with ZnS and InS were modeled based on the measured optical

properties. As expected, the current collected would be higher by using these two alternative types of buffer layers.
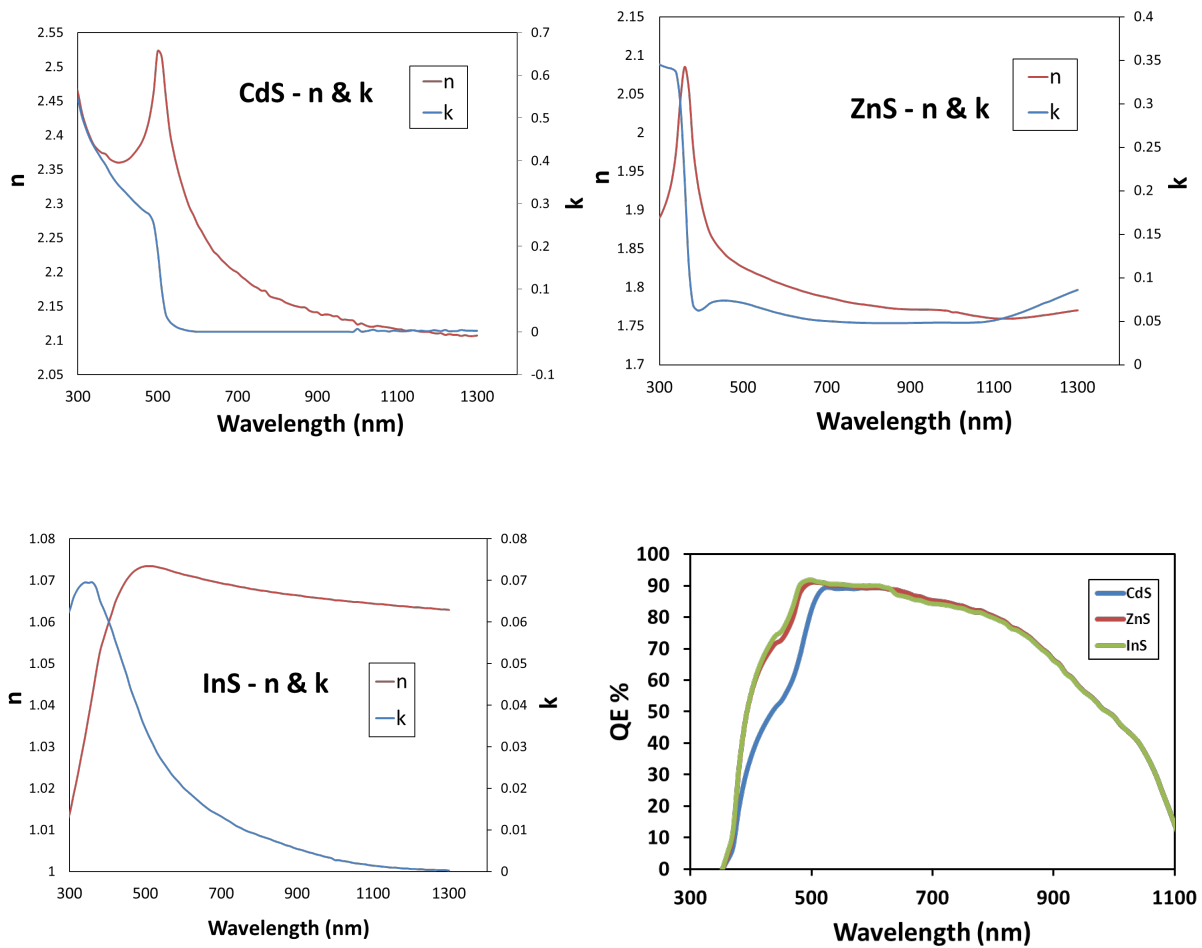

Figure 3.3.2: (n,k) values measured by ellipsometry for 3 different buffer layers and modeled QE for 3 different buffer layers.

3.4. Task #4 and Task #9 – *AR Filter*

Results on these Tasks were reported in the following RPPR-2 reports
- **Report 1**: perform optical modeling in the design of an anti-reflection (AR) coating working in tandem with the front contact to trap the light inside the cell.
- **Report 2**: started deposition of these AR coatings on 0.7 mm and 2 mm layers.
- **Report 3**: Successfully deposited new 2-layer, 3-layer and 4-layer AR filters on ultra-thin CIGS solar cells and demonstrated enhanced current generation; Successfully deposited, studied and modeled a variety of 2-layer, 3-layer and 4 layer AR filters based on MgF_2, HfO_2, Al_2O_3, SiO_2, ZrO_2, TiO_2; Developed an optical model to include the effect of the AR filter on the device efficiency
- **Report 4**: study the effect of AR coating on 0.5 um CIGS, the impact of SnO_2 back contact on the reflection
- **Report 5**: optical modeling and Quantum Efficiency predictions for CIGS, as well as to do optical enhancement of ultra-thin CIGS solar cells using multi-layered antireflection coatings
- **Report 7**: study multi-layer AR coatings deposition and optimization by RTSE
- **Report 8**: demonstrated ability to control the deposition of AR filter in real time via RTSE

A summary of the main results can be found below

3.4.1. Deposition and modeling of a variety of 2-layer, 3-layer and 4 layer AR filters based on MgF_2, HfO_2, Al_2O_3, SiO_2, ZrO_2, TiO_2.

Spectroscopic ellipsometry (SE) was used to characterize each layer in the CIGS solar cell structure and the optical properties were used to model the quantum efficiency, reflectance, transmittance, and the absorption losses in each layer. Figure 3.4.1 shows the optimization procedures for the thicknesses of two-layer anti-reflective coatings in an ultra-thin CIGS solar cell with 500 nm CIGS absorber layer and molybdenum back contact. The quantum efficiency, reflectance, and transmittance spectra have been determined, whereby the latter is the amount of light lost by absorption in the molybdenum layer due to the low reflectivity of the CIGS/Mo interface. This optical loss can be reduced either by using a spacer layer of a material such as SnO_2:F, ITO, or ZnO, or by using a back contact of higher reflectivity with desirable electrical properties such as ZrN, HfN, or TiN. On the other hand, reflectance losses can be reduced significantly using anti-reflective coatings. Anti-reflective (AR) coatings of 2 layers, 3 layers, and 5 layers have all been modeled and *optimized with respect to short circuit current density*. While 2- and 3-layer AR coatings significantly reduce reflectance across the wavelength range of operation of the solar cell, 5-layer AR coatings can theoretically decrease reflectance losses even more. However, this is valid only for planar-smooth interfaces. In the case of multilayer AR coatings, scattering can arise from rough interfaces and reduce the quality of the AR effect, and thus reduce the light delivered to the active layers.

For the *2-layer AR* structures investigated as shown in Fig. 3.4.1, the highest short circuit current density was predicted for: $MgF_2(120$ nm$)/HfO_2(200$ nm$)$ which gives $J_{sc\ max.} = 35.6$ mA/cm^2. Many structures were also investigated for the *3-layer AR* coatings, and the highest short circuit current density was found to be for the structure $MgF_2(104$ nm$)/HfO_2(63$ nm$)/ZrO_2(140$ nm$)$ with $J_{sc\ max.} = 35.7$ mA/cm^2. Finally, for the *5-layer AR* coating, several structures were investigated and the structure with the highest J_{sc} was found to be: $MgF_2(104$ nm$)/HfO_2(63$ nm$)/ZrO_2(118$ nm$)/HfO_2(16$ nm$)/ZrO_2(23$ nm$)$.
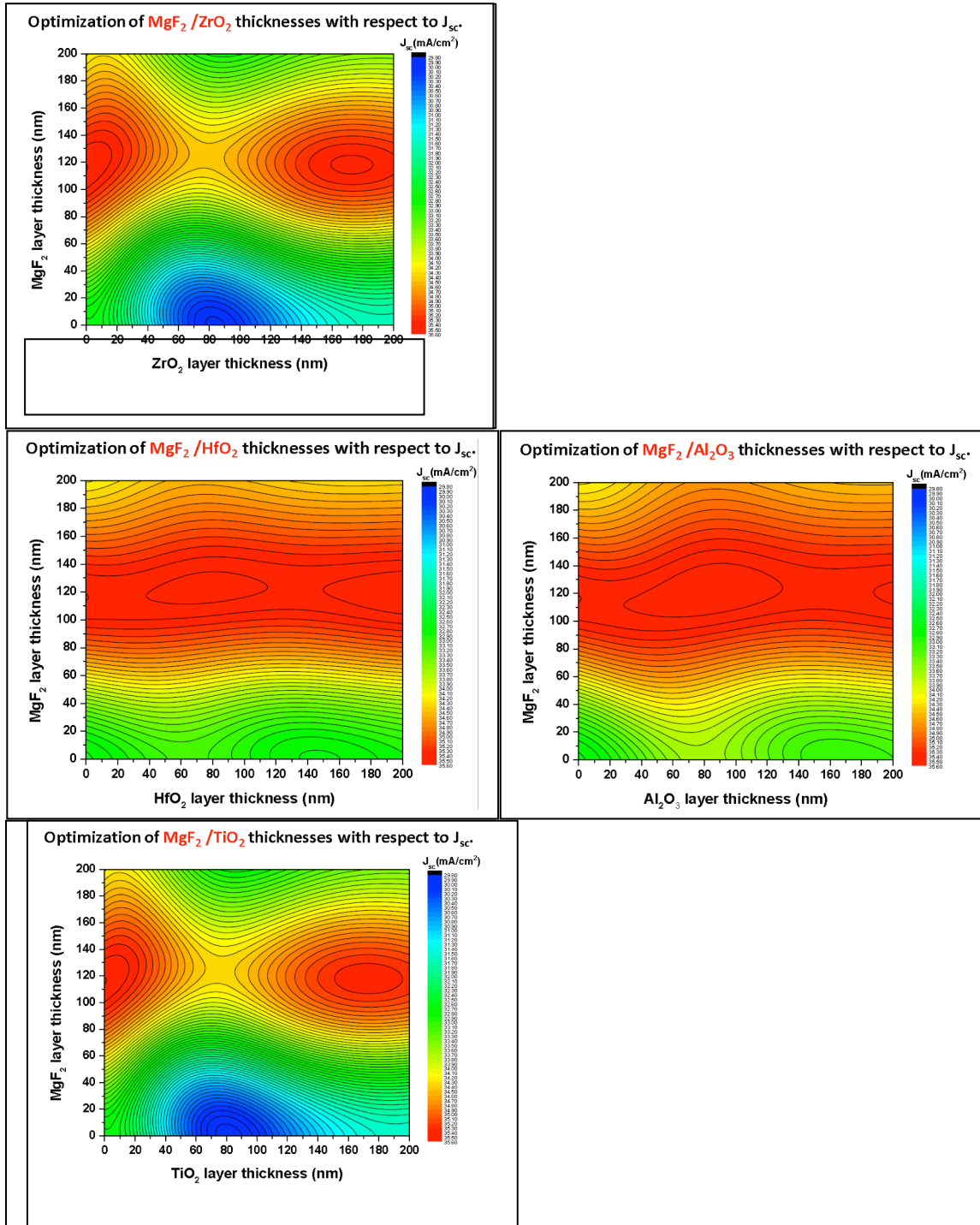
Figure 3.4.1: Optimization of two layer anti-reflective (AR) coatings; materials investigated include MgF_2, ZrO_2, HfO_2, Al_2O_3, SiO_2, and TiO_2.

The quantum efficiency, reflectance, and transmittance for the optimized two, three, and five layer AR coating structures were determined for additional guidance.

5-layer AR coatings were also modeled and optimized for TiN, ZrN and HfN back contacts. Structures with HfN back contacts seemed to have the highest short circuit current density and the AR-structure of: $MgF_2/HfO_2/ZrO_2/HfO_2/ZrO_2$ was found to give the highest current density with **J_{sc} = 36.6 mA/cm^2 for HfN back contact**. The corresponding quantum efficiency, reflectance, and transmittance for the two structures have been reported earlier. Significant decrease in transmittance (or back contact absorbance) loss was observed.

3.4.2 Optical modeling of anti-reflection coatings for solar cells with 0.5 mm CIGS absorber layer and Mo back contact

The effect of using a bi-layer AR coating on the simulated J_{SC} in a solar cell with 0.5 μm ultra-thin CIGS absorber layer was studied. The materials considered for the AR coating were MgF_2 and HfO_2. First, simulations were performed based on the SE deduced optical model shown in Fig. 3.4.2. A range of thicknesses for MgF_2 and HfO_2 were chosen for the simulation in order to locate the point where J_{SC} is maximized. The result is presented in Fig. 3.4.3. The maximum in J_{SC} was obtained for a MgF_2 thickness of 118 nm and a HfO_2 thickness of 200 nm. This approach to simulation helps in expediting the optimization of solar cells by estimating the required layer thicknesses even before any experiments are carried out.
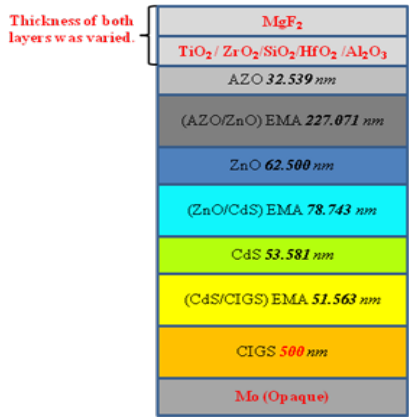

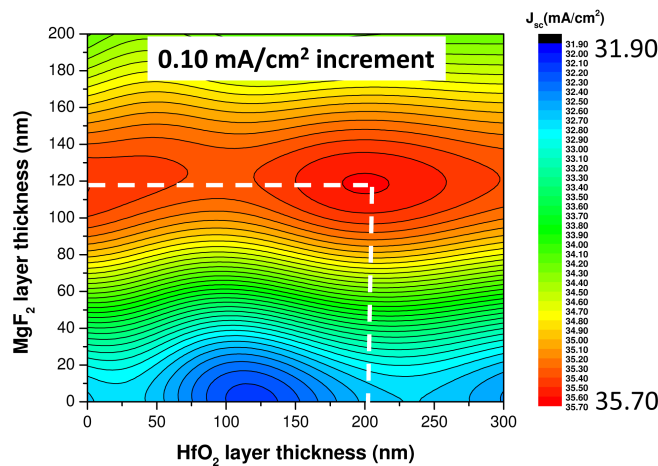**Fig. 3.4.2**: SE deduced optical model used for EQE/J_{SC} simulations.

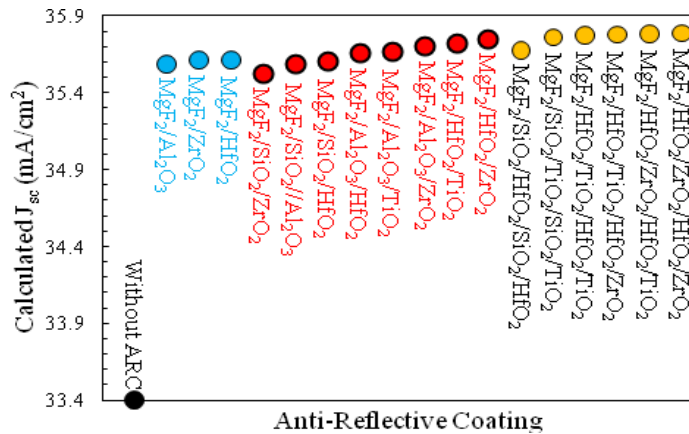**Fig. 3.4.3:** Identification of optimum two-layer AR from EQE/J_{SC} simulations.

Fig. 3.4.4: Calculated J_{SC} for optimum 2-layer, 3-layer, and 5-layer antireflection coatings on a CIGS solar cell with a 0.5 μm absorber layer.

J_{SC} were simulated for 2-layer, 3-layer and 5-layer antireflection coatings on a solar cell with 0.5 μm CIGS. The materials incorporated into these AR coating simulations were MgF_2, HfO_2, ZrO_2, TiO_2, Al_2O_3, and SiO_2. The results are shown in Fig. 3.4.4. It can be seen from the figure that although 2-layer coating improves J_{SC} significantly over no coating, there is only a small improvement in going from 2-layer coating to 5-layer coating.

3.4.3. Bi-layer AR coating on a solar cell with 0.5 μm CIGS

A bi-layer AR coating (MgF_2/HfO_2) with layer thicknesses optimized by simulation was deposited on the solar cell with 0.5 μm CIGS. The measured reflectance of the cell before and after the coating is shown in Fig. 3.4.5. Fig. 3.4.6 shows the EQE of the same cell before and after the bi-layer coating. The efficiency of the cell increased from 9.02 % to 10.10 % due to the coating.
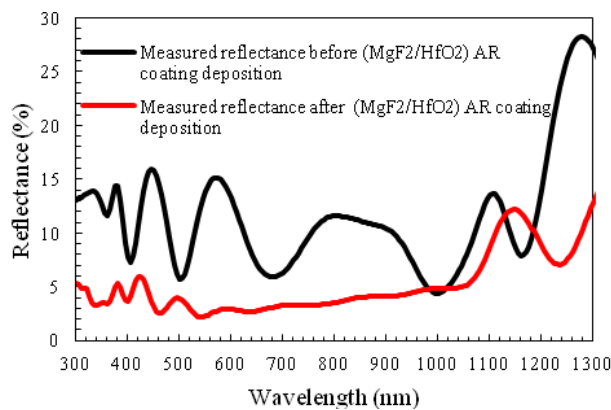

Fig. 3.4.5: Measured reflectance of a solar cell with 0.5 μm CIGS before and after bi-layer (MgF_2/HfO_2) AR coating.

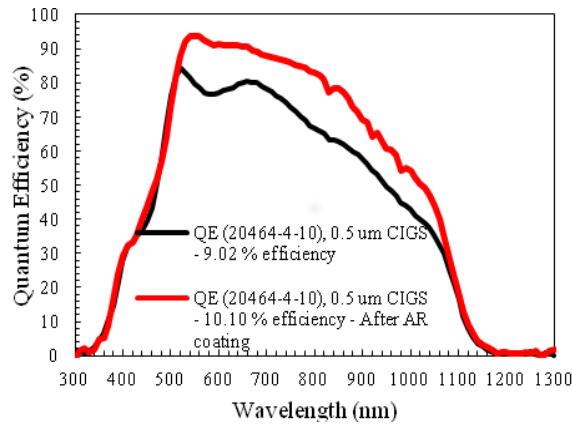**Fig. 3.4.6**: Measured EQE of a solar cell with 0.5 μm CIGS before and after bi-layer (MgF_2/ HfO_2) AR coating.

3.4.4. Optimization of reflector material: MgF_2/(0.5 μm CIGS cell)/SnO_2:F/reflector

J_{SC} data were simulated for a MgF_2 coated solar cell with 0.5 μm CIGS, different reflector materials, and a SnO_2:F spacer layer of different thicknesses. Three different spacer layer thicknesses were considered: d_o (= 0 nm), d_1 and d_2 (first and second optima). The results of these simulations are shown in Figure 3.4.7. In all cases, a dielectric spacer layer improves light collection by 0.5 μm CIGS. The best reflector materials are the noble metals; however, films of these materials are not stable at the deposition temperature, as they will react with the spacer layer and/or CIGS. The best reflector that is stable under the CIGS deposition conditions is HfN. Until a regular supply of nitrides is available, Ag films are being deposited on the back surfaces of the glass after fabrication of solar cells with ultra-thin CIGS on TCO-coated glass. These Ag films serve as interim reflectors. In this case, the spacer consists of the glass and the TCO stack.
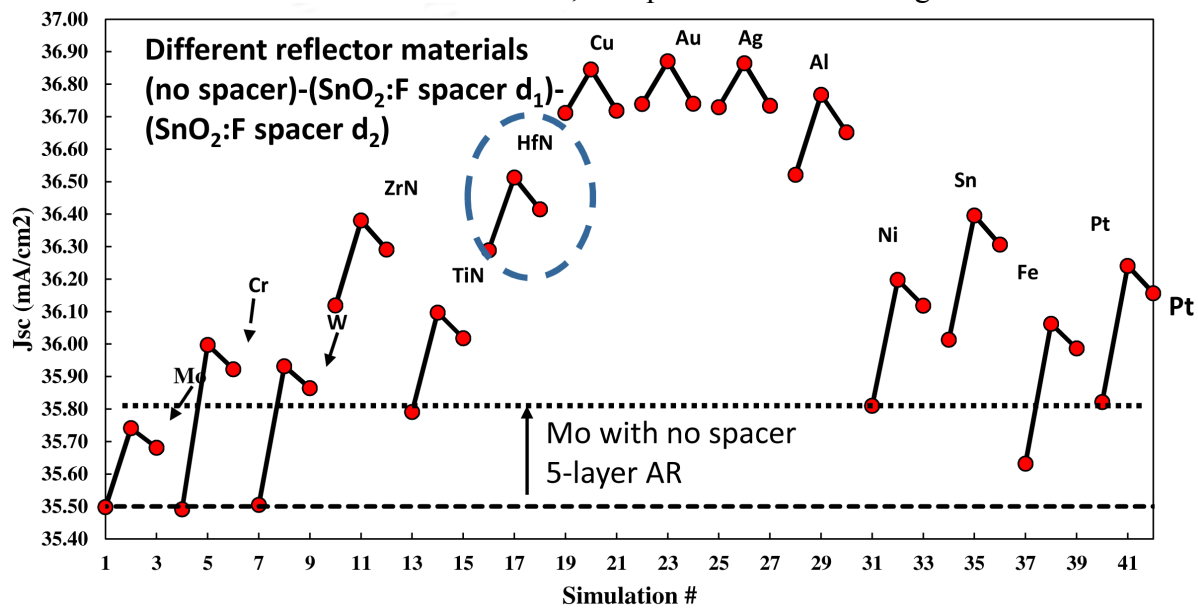

Fig. 3.4.7: J_{SC} predicted for different reflector materials and three SnO_2:F spacer layer thicknesses d_o, d_1, and d_2.

3.4.5. Optimization of Reflector Thicknesses: MgF$_2$/(0.5 µm CIGS cell)/SnO$_2$:F/glass/Ag

Simulations were performed for J$_{SC}$ with a range of MgF$_2$ and SnO$_2$:F layer thicknesses for the structure MgF$_2$/(0.5 µm CIGS cell)/SnO$_2$:F/glass/Ag. The optical model used for these simulations is shown in Fig. 3.4.8. The resulting optimization map is shown in Fig. 3.4.9 which indicates that the best SnO$_2$:F and MgF$_2$ layer thicknesses are 235 nm and 114 nm, respectively.
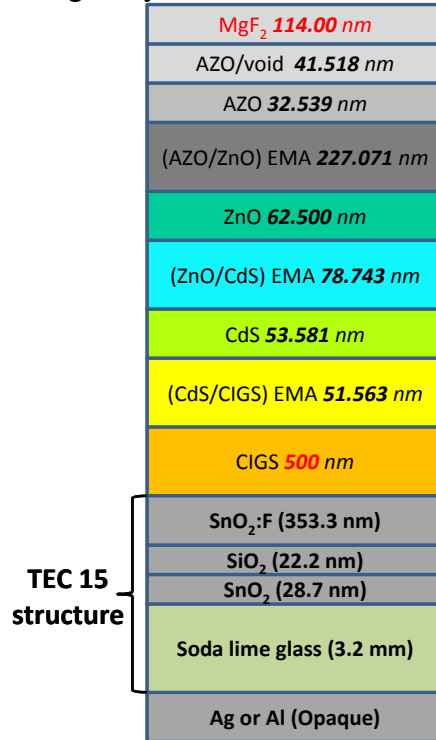

Fig. 3.4.8: Optical model of a solar cell with 0.5 µm CIGS. This model is used for J$_{SC}$ simulations with different MgF$_2$ and SnO$_2$:F layer thicknesses.
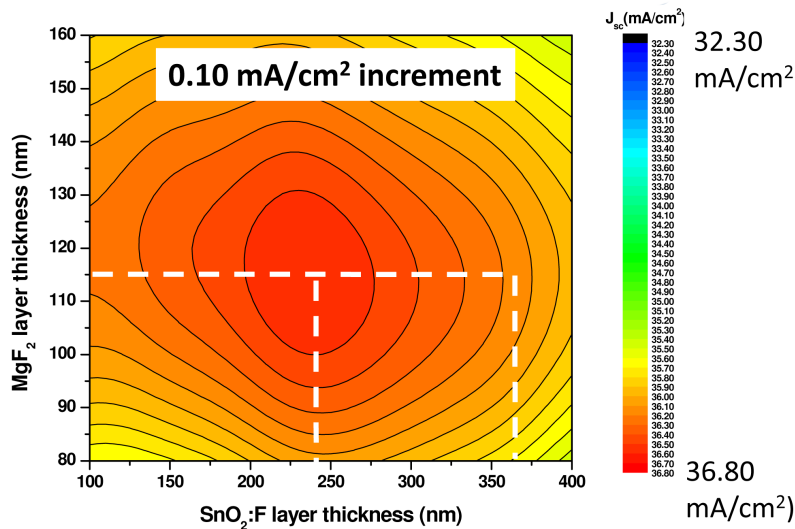

Fig. 3.4.9: Optimization map for a solar cell with 0.5 µm CIGS and different MgF$_2$ and SnO$_2$:F layer thicknesses.

3.4.6 Solar Cells with Thin Cu(In$_{1-x}$Ga$_x$)Se$_2$: Optical Modeling and Quantum Efficiency Predictions

I. Introduction

In order to maximize the collected photo-generated carriers in ultra-thin CIGS solar cells through optical means, in-depth analysis of the cell's optical structure is required as a starting point. Such analysis is best undertaken using spectroscopic ellipsometry (SE). SE is a non-invasive, optical technique that can serve as a precise probe of individual layer optical properties and multi-layer structure. Previous work has been reported on theoretical quantum efficiency (QE) simulations for CIGS devices based on layer optical properties and device structure measured using variable-angle SE. Very good agreement was found between simulated and measured QE spectra for a standard CIGS cell deposited on Mo, indicating minimal electronic losses. As a result, the QE spectrum for a CIGS device can be predicted theoretically from the optically deduced light absorption in the active components. Since J_{sc} can be directly calculated from QE spectra, then predicted QE and J_{sc} can be compared with the experimental values to understand electronic losses in the ultra-thin CIGS solar cells.

In this study, CIGS solar cells with thin absorbers were deposited and characterized using SE. Optical modeling was then applied to predict QE spectra and J_{sc} values assuming no electronic losses. Comparing calculated QE spectra with the ones measured experimentally, electronic losses were observed. By dividing the absorber layer into several sub-layer components (e.g.: junction, bulk, and back contact regions), the contribution of each component of the absorber to the photo-generated current can be estimated. Based on this separation, the origin of the electronic losses can be identified.

Also in this study, applying the same optical modeling techniques, the maximum obtainable J_{sc} values are calculated for different thicknesses both without and with AR coatings. Furthermore, optical modeling was also applied to predict the maximum obtainable J_{sc} values in thin CIGS solar cells made with different Ga contents x, assuming uniform layer composition. Although the optimum performance in standard CIGS devices is obtained for absorbers with x ~ 0.3, we suggest that such an optimum may not be retained upon thinning the CIGS.

II. Experimental details

CIGS solar cells with 2.2, 0.73, 0.50 and 0.36 μm absorber layer thicknesses were fabricated on molybdenum (Mo) coated soda-lime glass (SLG) using a 3-stage CIGS co-evaporation process. The device structure includes the following: soda lime glass (SLG), dc-sputtered Mo back contact (~ 1 μm), CIGS absorber layer, chemical-bath-deposited (CBD) CdS (50-60 nm), RF-sputtered bi-layer ZnO/ZnO:Al (0.3-0.4 μm), and electron beam evaporated Ni/Al/Ni grids for a total cell area of 0.5 cm^2, as defined by mechanical scribing. CIGS layer thicknesses were measured by profilometry and by SE, and AR coatings (MgF$_2$ and MgF$_2$/HfO$_2$) were deposited in an e-beam evaporator.

The optical gains/losses were calculated using a model developed on a C++ platform which calculates electric-field profiles and, thus, light absorption in each layer of the CIGS solar cell structure, assuming coherent propagation of optical plane waves without scattering. SE was first used to extract the optical properties of each layer of the standard CIGS device structure. For the Mo and CIGS optical properties, real time and in situ measurements were performed in order to measure and correct for surface roughness and to avoid oxidation. SE was then applied to analyze the complete CIGS solar cell structure by fitting the experimental SE data with an

optical model to extract (i) the thickness of each layer, (ii) a void fraction as needed in each layer, and (iii) the thickness and composition of each interface roughness layer.

III. Results

Fig. 3.4.10 shows optically simulated and measured QE spectra for a standard solar cell with a 2.2 μm CIGS absorber layer. The dependence of the best η PV parameters on the CIGS thickness shows that the expected decrease in J_{sc} is observed, but FF also decreases for absorbers thinner that 0.7 μm due to higher shunt conductance. QE measurements were acquired and compared to optically modeled spectra. Fig. 3.4.11 shows the predicted maximum and experimentally obtained J_{sc} values with and without AR coatings.
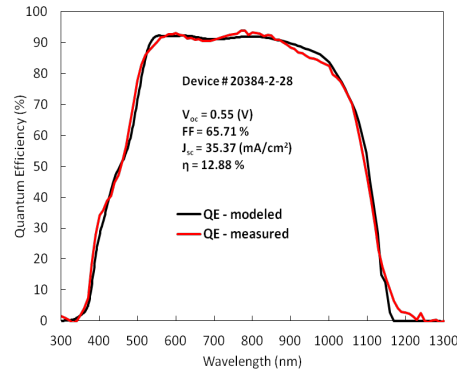

Fig. 3.4.10: Measured (red) and optically simulated quantum efficiency (black) obtained by applying ex-situ SE analysis and optical modeling to a standard solar cell with a 2.2 μm CIGS absorber layer.

The difference in spectral shapes in the 400-500 nm wavelength range is due to variation in the CdS layer thickness. In the long-wavelength region, QE spectra show a decrease in photo-generated charge carrier collection attributed to incomplete light absorption in the absorber layer. In order to evaluate optical and electronic losses, however, the maximum obtainable QE is optically modeled for each device and compared to the measured QE.

For all solar cells with thin CIGS, the optically modeled QE spectra show higher charge carrier collection than the measured spectra in the wavelength range > 520 nm. The differences between the two spectra are due to electronic losses. The lower QE for red photons implies a shorter collection length. The improved QE fits, obtained assuming an inactive layer adjacent to the Mo back contact, indicate a lower charge carrier diffusion length.

Whereas the recombination losses are mainly occurring near the Mo back contact, electronic losses near the junction are also occurring due to decrease in the QE spectra in the wavelength range of 450-600 nm.

To reduce effects of shunting on device efficiency, one may suggest increasing the thickness of the CdS layer. In a previously reported study, however, an increase in CdS layer thickness contributed only to greater optical losses, which in return reduced J_{sc} for the solar cells, but without improving FF or V_{oc}. Recombination losses at the back contact and short diffusion length can be improved by introducing a higher Ga-gradient toward the back contact or a thin layer of $CuGaSe_2$. Such gradients create a back-surface-field due to increase in conduction band energy level, which improves collection as well as FF and V_{oc}.
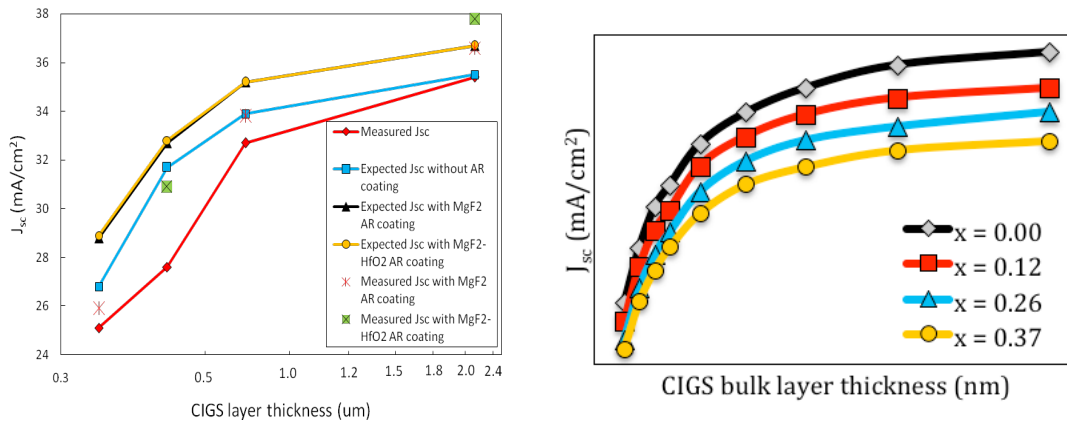
Fig. 3.4.11: Measured and optically simulated J$_{sc}$ values for CIGS solar cells with standard and thin absorbers with and without AR coatings. Right: Measured QE spectra for CIGS solar cells with a standard 2.2 µm absorber layer, and thin 0.73, 0.50 and 0.36 µm absorbers.

To clarify the limits of obtainable J$_{sc}$ in ultra-thin CIGS solar cells with Mo back contact, optically predicted J$_{sc}$ values are shown in Fig. 3.4.11 for thin CIGS solar cells with uniform absorbers of different Ga contents, assuming no electronic losses. The predicted values are based on device structures determined using SE analysis. The optical properties of the CIGS films as functions of Ga ratio have been reported previously. A more rapid decrease in J$_{sc}$ is predicted as the absorber thickness becomes thinner than 0.5 µm. As one can see in Figure 3.4.12, in reality one has also ot take into account electronic losses. Thus, a practical choice for thinning CIGS, is an absorber of ~ 0.5 µm. Clearly in order for ultra-thin CIGS solar cells to scale-up in solar module manufacturing, several issues require further investigation to improve photo-generated current collection as well as achieve high electronic performance.
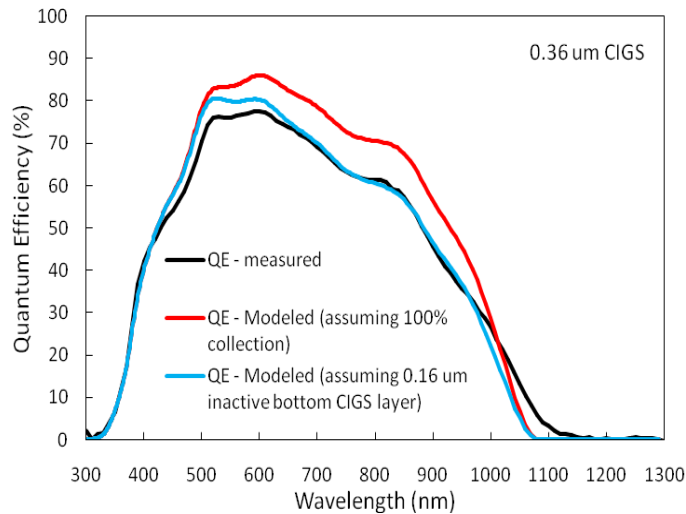

Fig. 3.4.12: Comparison of experimentally measured and optically modeled QE spectra for CIGS solar cell with 0.36 µm absorber layer.

3.4.7. Optimizing the Anti-reflective coating during deposition

RTSE measurements were carried out to monitor the average reflectance from the CIGS cell structure during the course of deposition of anti-reflective layers. This close monitoring aids in optimizing the thickness and structure of the AR layers. For a thick CIGS layer (2um), a layer of MgF_2 is sufficient to reduce the top reflection. Figure 3.4.13 records the reduction of reflectance of the device across the spectral wavelength during the course of deposition of the AR layer.
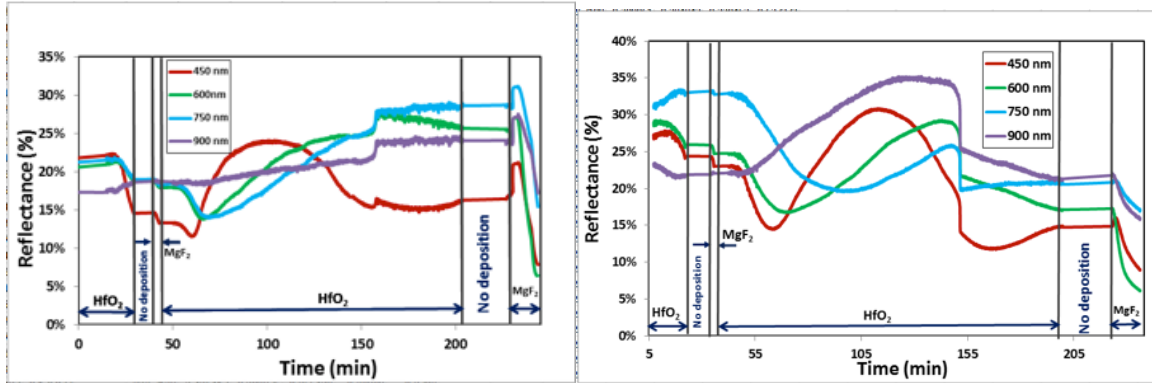

Figure 3.4.13: Real time reflectance measurement during the deposition of MgF_2 AR layer on a thick (2μm) CIGS cell structure. **Figure 3.4.14 a)**: Real time reflectance measurement during the deposition of multi-layer AR coating ($HfO_2/MgF_2/ HfO_2/MgF_2$) on a CIGS structure of thickness 1000nm.

However with the reduced thickness of CIGS layer, the reflection from the first surface cannot be completely cancelled through destructive interference with the weaker reflection from the top surface. Thus the characteristics of the single quarter wave layer can be improved by adding a high index half wave layer between MgF_2 layer and the substrate to broaden the characteristics.
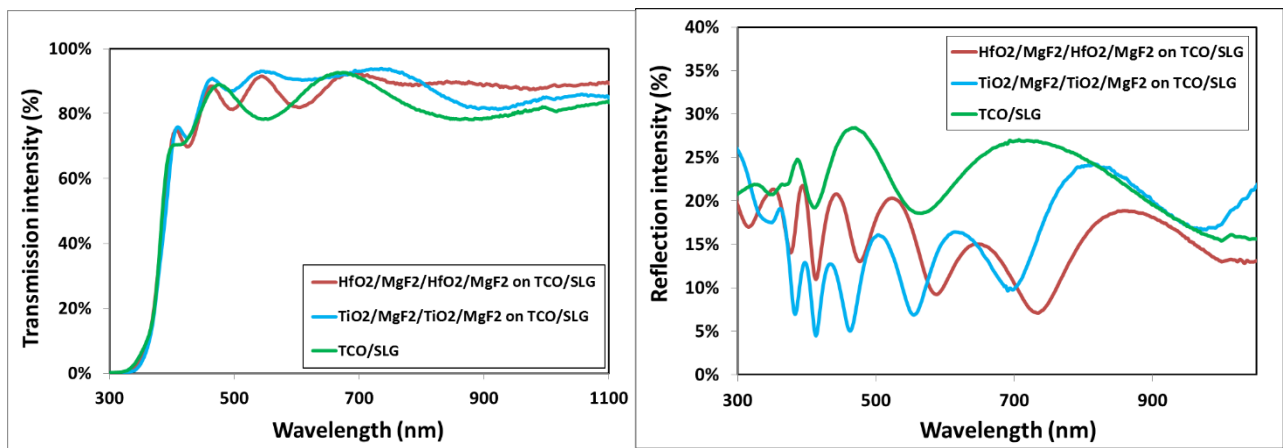

Figure 3.4.15: Measured reflectance and transmittance spectra of a standard TCO structure on SLG with different multi-layer AR structure.

With multi-layers, there are multiple minimum reflection points at different wavelengths and the average reflectance is comparatively reduced. Figure 3.4.14 shows the real time reflectance measurement during deposition of multi-layer AR coatings on ultra-thin CIGS cells with different absorber layer thickness. Lower rates of deposition of HfO_2 considerably increased the

duration of deposition of the multi-layer AR structure on ultra-thin CIGS cell. This led to the increase of substrate temperature and increased diffusion into cell structure slightly affecting the performance of the device. In parallel to HfO_2, other materials were tested and used for multi-layer AR coating along with MgF_2. Figure 3.4.14 compares the transmittance curve and reflectance curve for the two multi-layer AR coating structures on TCO substrate. The TCO's were deposited directly on soda lime glass (SLG). This study was performed to evaluate the possible substrate dependence of the optical properties of the AR coatings as Al:ZnO being the top most layer of the CIGS solar cell.

RTSE measurements were also carried out to monitor the average reflectance of these two multi-layer AR structure on ultra-thin CIGS cells. Ex-situ reflectance measurements of the CIGS devices has also been measured of devices before and after the deposition of the multi-layer structure to correlate to the RTSE measurements. Figure 3.4.16 and 3.4.17 shows the real time reflectance measurement of the ultra-thin CIGS devices during the course of deposition of multi-layer structure correlated with the ex-situ reflectance measurement.
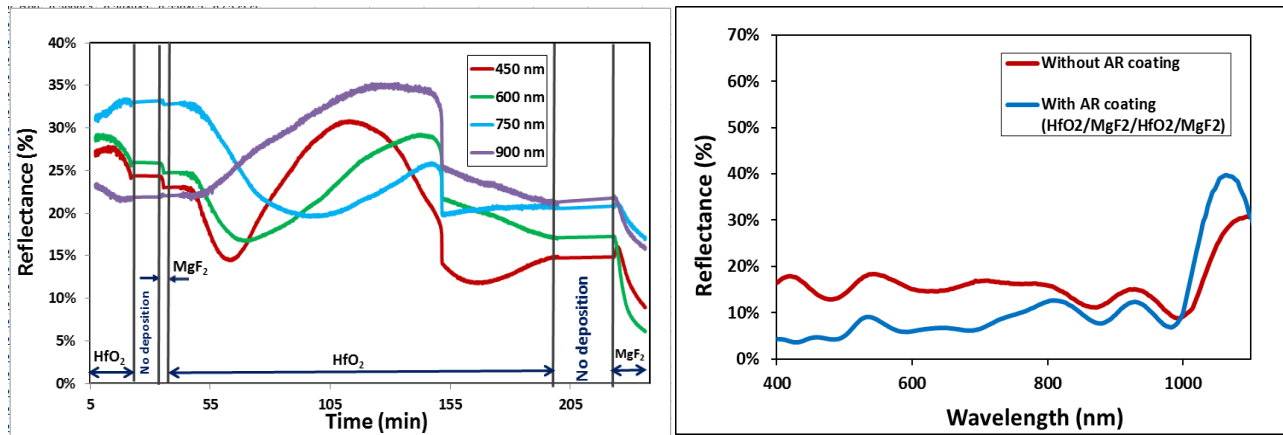

Figure 3.4.16 Real time reflectance measurement during deposition of (HfO_2/MgF_2/ HfO_2/MgF_2) AR layer on ultra-thin CIGS (600 nm) cell. Reflectance measurements of the device before and after AR coating.

Figure 3.4.17 Real time reflectance measurement during deposition of (TiO_2/MgF_2/TiO_2/MgF_2) AR layer on ultra-thin CIGS (600 nm) cell. Reflectance measurements of the device before and after AR coating.

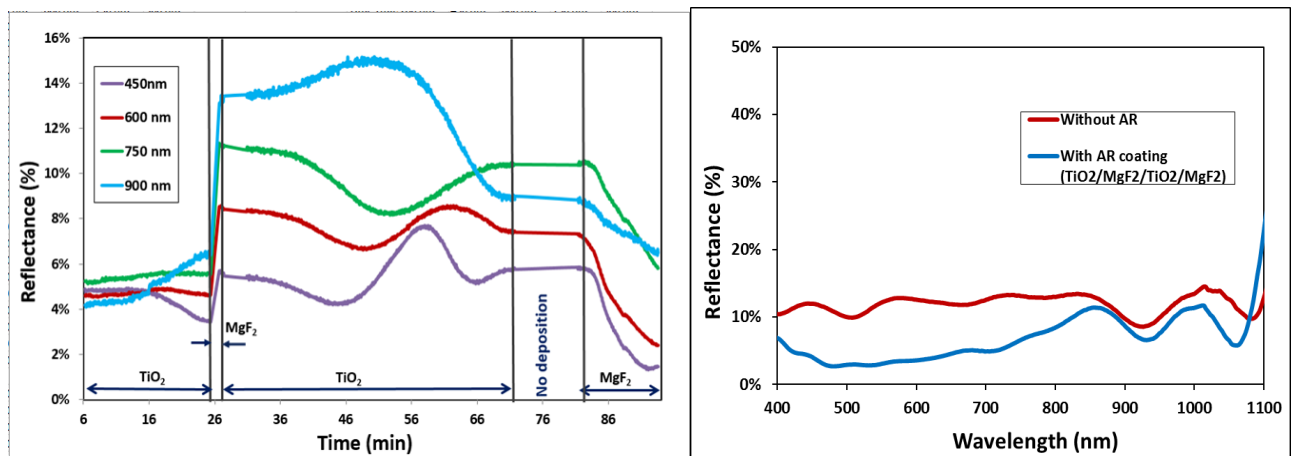RTSE measurements were carried out to obtain relative reflectance of ultra-thin CIGS device on alternative back contacts with the multi-layer AR (TiO_2/MgF_2/TiO_2/MgF_2) coatings. The reflection intensity of the layers was closely monitored for different wavelengths in-situ during the deposition of AR coating on CIGS device. Real time measurements aid to optimize the dimensions of the different AR layers so as to reduce the reflection for a specific spectral range thus leading a reduction in the average reflectance. Figure 3.4.18-3.4.20 compares the real time reflectance measurement for multi-layer AR coating on ultra-thin CIGS device on alternative back contacts.
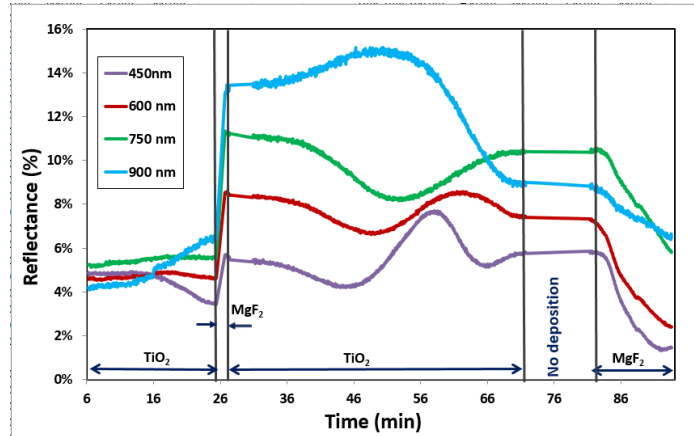

Figure 3.4.18 Real time reflectance measurement of multi-layer AR coating on CIGS device with Mo back contact
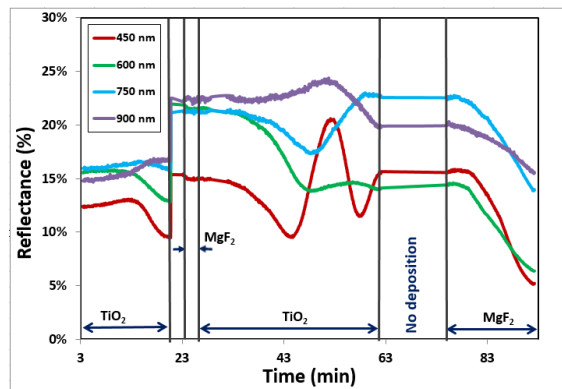

Figure 3.4.19 Real time reflectance measurement of multi-layer AR coating on CIGS device with VN back contact
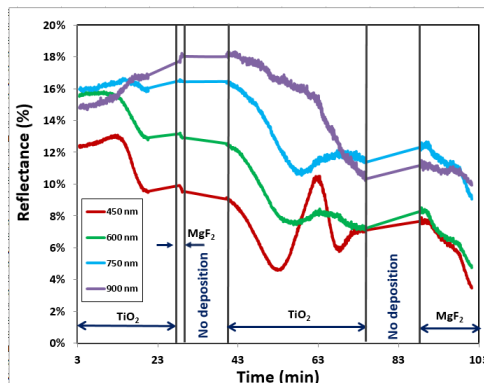

Figure 3.4.20 Real time reflectance measurement of multi-layer AR coating on CIGS device with ZrN back contact.

4. Conclusions

The main objective of this proposal was to use several pathways to reduce the production cost of CIGS PV modules and therefore the levelized cost of energy (LCOE) associated with this technology. Three high cost drivers were identified, nominally:

7) Materials cost and availability
8) Large scale uniformity
9) Improved throughput

These three cost drivers were targeted using the following pathways:

7) Reducing the thickness of the CIGS layer while enhancing materials quality
8) Developing and applying enhanced in-situ metrology via real time spectroscopic ellipsometry
9) Looking into alternative heterojunction partner, back contact and AR coating

Eleven main Tasks were then defined to achieve these goals (5 in Phase 1 and 6 in Phase 2), with 11 Milestones and 2 Go/No-go decision points at the end of Phase 1. The key results are summarized below

4.1. Task #1 and Task #6 – *Back Contact*
4.1.1. Key results

- Demonstrated enhanced current with ZrN back contact compared to Mo back contact for 0.5 um CIGS
- Demonstrated 8.5% efficiency solar cell with Ag/Glass/TCO back contact for 0.5 um CIGS
- Successfully studied the effect of sodium on ultra-thin CIGS

4.1.2. Milestones

There was one Milestone for these tasks (M7), which was to identify best material and best design. This was successfully done by studying several transition metal nitrides, and several transparent conductive oxides in combination with a back mirror. At this stage, the best choice still remains molybdenum. The transition metal nitrides have higher current but l

4.2. Task #2 and Task #7 – *Reducing Thickness*
4.2.1. Key results

- Implemented RTSE as an effective *in-situ* and real time tool for controlling 3-stage process deposition
- Demonstrated influence of gallium content on the growth process and the need for controlling its content in ultra-thin films
- Demonstrated capacity to use mapping SE to correlate extracted results with device performance
- Demonstrated the use of nano-DLTS for identifying activation energy of various trap levels, showing that they are systematically located at grain boundaries, but not present at every grain boundary
- Fabricated several high efficiency ultra-thin CIGS solar cells, notably a 13.2% cell for 0.73 um CIGS and a 10.4% cell for 0.55 um CIGS and a 9.1 % cell for a 0.35 um cell (baseline for these cells was 16% for 2 um CIGS). This is on par with the best ultra-thin CIGS solar cells ever reported.

4.2.2. Milestones

There were three Milestones for these tasks (M1, M4 and M8), which consisted in fabricating ultra-thin CIGS solar cells as well as enhancing the efficiency of the cell compared to our baseline process. This was successfully achieved for all thicknesses. For example, our 0.73 um device was 13.2% after modification of the process compared to 8% before. Note also that other groups who reported results on ultra-thin cells (such as NREL or Uppsala), have a much higher baseline efficiency than ours for 2 um (18.7% for NREL compare to 16% for us). It is also worth noting that even our 2 um cell was enhanced by the end of the project and went from 16% at the beginning of this project to 17.6% at the end of the project.

4.3. Task #3 and Task #8 – *Alternative buffer layers*

4.3.1. Key results

- Deposited alternative materials to CdS, such as ZnS and InS. Demonstrated higher current generation for both compounds
- Used alternative deposition method to CBD to deposit the materials, by using ALD
- Fabricated high efficiency solar cell using a 0.8 um CIGS and ZnS deposited by ALD. Demonstrated higher current generation compared to the CBD CdS reference cell (36 mA/cm^2 vs. 34 mA/cm^2) and higher efficiency (7.7% vs. 7.0%)

4.3.2. Milestones

There were three Milestones for these tasks (M2, M5 and M9), which consisted in depositing new materials for the buffer layer such as ZnS and InS, with alternative deposition process to CBD, such as ALD, sputtering or evaporation, and demonstrating higher current generation and higher efficiency with these alternatives. This was successfully achieved by depositing a ZnS buffer layer by ALD and achieving higher efficiency than for a CdS CBD deposited buffer layer.

4.4. Task #4 and Task #9 – *AR Filters*

4.4.1. Key results

- Successfully deposited and modeled of a variety of 2-layer, 3-layer and 4 layer AR filters based on MgF_2, HfO_2, Al_2O_3, SiO_2, ZrO_2, TiO_2. Demonstrated enhanced current generation compared to a single MgF_2 layer in all cases
- Successfully deposited and modeled high/low refractive indexes bilayer
- Modeled effect of AR coating on ultra-thin CIGS solar cell efficiency using a variety of back contact
- Successfully predicted QE spectrum based on SE measurements
- Successfully demonstrated capacity to use SE as a real time tool to optimize thickness of the AR filter for enhanced efficiency

4.4.2. Milestones

There were three Milestones for these tasks (M3, M6 and M10), which consisted in depositing different types of AR filters on ultra-thin cells and demonstrating enhanced efficiency compared to devices with only MgF_2. This was successfully achieved by depositing new 2-layer, 3-layer and 4-layer AR filters on ultra-thin CIGS solar cells and demonstrating enhanced current generation and efficiency.

4.5. Task #10 – *Full device development*

4.5.1. Key results

- Successfully deposited 0.75 um solar cell with 13.2% efficiency

4.5.2. Milestones

There was one Milestone for this task (M11), which consisted in depositing CIGS solar cells with various thicknesses and all enhancement implemented. This was nearly achieved by fabricating a 0.75 um solar cell with 13.2% efficiency compared to our 16% baseline for 2 um, and was achieved for the thicker cells by enhancing our baseline from 16% to 17.6% at the and of the project for the 2 um cell.

4.6. Go/No-Go decision

We had 2 Go/No-Go decision criteria at the end of Phase 1, which were both successfully completed

4.6.1. Go/No-Go criteria 1: *Develop a suitable deposition process enabling fabrication of a CIGS solar cell with a 0.5 mm CIGS layer and enhanced efficiency compared to that on same device before modification of the process*

    - Result: Successfully fabricated 0.6 mm CIGS solar cell with 12.1% efficiency (without AR coating). This is on par with the best ultra-thin CIGS solar cells ever reported by NREL, but with a much lower baseline efficiency (16% vs 18.7%). This is much better than our device efficiency before modification of the process (8%).

4.6.2. Go/No-Go criteria 2: *Develop a suitable buffer layer that will allow us to fabricate a solar cell with higher current compared to reference CdS*

    - Result: Successfully deposited ZnS by ALD on a 0.8 mm CIGS device and demonstrated enhanced current generation

4.7. Task #5 and #11: Publications

As part of the project, we published several papers in peer reviewed journals and conference proceedings, which are listed below.

4.7.1. Publications associated with the contract

1.   V. Ranjan, R.W. Collins, and S. Marsillac
"Real time analysis of the evolution of the microstructure and optical properties of Cu(In,Ga)Se$_2$ thin films as a function of Cu content"
Physica Status Solidi RRL 6 (1) (2012) 10–12.
2.   S. Marsillac, H. Khatri, K. Aryal, R.W. Collins
"Properties of Cu(In,Ga)Se$_2$ Thin Films and Solar Cells deposited by Hybrid Process"
International Journal of Photoenergy 2012 (2012) 385185.
3.   K. Aryal, H. Khatri, R.W. Collins and S. Marsillac
"In-situ and ex-situ studies of molybdenum thin films deposited by rf and dc magnetron sputtering as a back contact for CIGS solar cells"
International Journal of Photoenergy 2012 (2012) 723714.
4.   S.A. Little, V. Ranjan, R.W. Collins, S. Marsillac
"Growth analysis of (Ag,Cu)InSe$_2$ thin films via real time spectroscopic ellipsometry"
Applied Physics Letters 101(23) (2012) 231910.
5.   P. Aryal, D. Attygalle, P. Pradhan, N. J. Podraza, S. Marsillac, R.W. Collins
"Large-area compositional mapping of Cu(In1−xGax)Se$_2$ materials and devices with spectroscopic ellipsometry"
IEEE J. Photovolt. 3(1) (2013) 359–363.
6.   D. Attygalle, V. Ranjan, P. Aryal, P. Pradhan, S. Marsillac, N.J. Podraza, R.W. Collins

"Optical Monitoring and Control of Three-Stage Coevaporated Cu(In1-xGax)Se$_2$ by Real-Time Spectroscopic Ellipsometry"
IEEE J. Photovolt. 3(1) (2013) 375-80.

7.	V. Ranjan, T. Begou, S. Little, R. W. Collins, and S. Marsillac
"Non-destructive optical analysis of band gap profile, crystalline phase, and grain size for Cu(In,Ga)Se$_2$ solar cells deposited by 1-, 2-, and 3-stage co-evaporation"
Progress in Photovoltaics: Research and Applications 22(1) (2014) 77–82.

8.	P. Aryal; P. Pradhan; D. Attygalle; A. Ibdah; K. Aryal; V. Ranjan; S. Marsillac; N.J. Podraza; R.W. Collins
"Real-Time, In-Line, and Mapping Spectroscopic Ellipsometry for Applications in Cu(In$_{1-x}$Gax)Se$_2$ Metrology"
IEEE Journal of Photovoltaics 4(1) (2014) 333-339.

9.	PK. Paul, D.W. Cardwell, C.M. Jackson, K. Galiano, K. Aryal, J.P. Pelz, S. Marsillac, S.A Ringel, T.J. Grassman, A.R. Arehart
"Direct nm-scale spatial mapping of traps in CIGS"
IEEE Journal of Photovoltaics 5(5) (2015) 1482-1486.

4.7.2. Conference proceedings associated with the contract

1.	S. Marsillac and R.W. Collins
"Spectroscopic Ellipsometry: Metrology for Photovoltaics from the Nano to the Giga"
SPIE photonic West
San Francisco, January 21-26 2012.

2.	R.W Collins, L. Dahal, Z. Huang, D. Attygalle, P. Aryal, J. Chen, M. Sestak, N. Podraza, A. Nemeth, P. Petrik, G. Juhasz, C. Major, M. Fried, S. Marsillac
"Large Area Imaging/Mapping Spectroscopic Ellipsometry for Multilayer Analysis in Thin Film Photovoltaics"
Spring MRS Conference
San Francisco, April 9-13 2012.

3.	D. Attygalle, P. Aryal, P. Pradhan, N. Podraza, R.W. Collins, V. Ranjan, H. Khatri, S. Marsillac.
"Optical Monitoring and Control of Cu(In,Ga)Se$_2$ Thin Film Deposition: Analysis of Copper Transitions in Three-Stage Co-Evaporation"
Spring MRS Conference
San Francisco, April 9-13 2012.

4.	S. Little, V. Ranjan, R.W. Collins and S. Marsillac
"Analysis of (Ag,Cu)(In,Ga)Se$_2$ solar cells deposited by a hybrid process"
38th IEEE Photovoltaic Specialists Conference
Austin, USA, June 3-8 2012.

5.	S. Marsillac, V. Ranjan, K. Aryal, S. Little, Y. Erkaya, G. Rajan, P. Boland, D. Attygalle, P. Aryal, P. Pradhan, R.W. Collins
"Toward ultra thin CIGS solar cells"
38th IEEE Photovoltaic Specialists Conference
Austin, USA, June 3-8 2012.

6.	V. Ranjan, K. Aryal, S. Little, Y. Erkaya, G. Rajan, P. Boland, D. Attygalle, P Aryal, P. Pradhan, R.W. Collins, S. Marsillac
"Real time analysis of ultra thin CIGS thin film deposition"

38th IEEE Photovoltaic Specialists Conference
Austin, USA, June 3-8 2012.

7. H. Khatri, K. Aryal, and R.W Collins, S. Marsillac
    "Electronic and structural properties of copper selenide ($Cu_{2-x}Se$) thin films as determined by in-situ real-time and ex-situ characterization"
    38th IEEE Photovoltaic Specialists Conference
    Austin, USA, June 3-8 2012.

8. K. Aryal, G. Rajan, Y. Erkaya, N. Hegde, P. Boland, V. Ranjan, R.W. Collins, S. Marsillac
    "Characterization of TCO deposition for CIGS solar cells"
    38th IEEE Photovoltaic Specialists Conference
    Austin, USA, June 3-8 2012.

9. Y. Erkaya, N. Hegde, K. Aryal, G. Rajan, P. Boland, V. Ranjan, H. Baumgart, R.W. Collins, S. Marsillac
    "Characterization of ZnS films deposited by ALD for CIGS solar cells"
    38th IEEE Photovoltaic Specialists Conference
    Austin, USA, June 3-8 2012.

10. S. Marsillac and R.W. Collins
    "Metrology for photovoltaics from the nanoscale to the gigawatt via spectroscopic ellipsometry"
    International Materials Society Conference
    Cancun, Mexico, August 5-12 2012.

11. G. Rajan, A.A. Ibdah, K Aryal, RW. Collins, S. Marsillac
    "Multi layered anti-reflective coatings for ultra-thin CIGS solar cells"
    39th IEEE Photovoltaic Specialists Conference
    Tampa, USA, June 16-21 2013.

12. K. Aryal, Y. Erkaya, G. Rajan, T. Ashrafee, A. Rockett, R.W. Collins, S. Marsillac
    "Comparative study of ZnS thin films deposited by CBD and ALD as a buffer layer for CIGS solar cell"
    39th IEEE Photovoltaic Specialists Conference
    Tampa, USA, June 16-21 2013.

13. K. Aryal, G. Rajan, T. Ashrafee, V. Rajan, P. Aryal, A. Rockett, R. Collins, S. Marsillac
    "Real time Spectroscopic Ellipsometry Studies of ultrathin CIGS films deposited by 1-stage, 2-stage and 3-stage co-evaporation process"
    40th IEEE Photovoltaic Specialists Conference
    Denver, USA, June 8-13 2014.

14. K. Aryal, G. Rajan, T. Ashrafee, V. Rajan, A. Rockett, R.W. Collins, S. Marsillac
    "Effect of selenium evaporation rate on ultrathin $Cu(In,Ga)Se_2$ films"
    40th IEEE Photovoltaic Specialists Conference
    Denver, USA, June 8-13 2014.

15. P. Pradhan, P. Aryal, A. Ibdah, P. Koirala, J. Li, N.J Podraza, AA. Rockett, S. Marsillac, RW Collins
    "Effect of Molybdenum Deposition Temperature on the Performance of $CuIn1-xGaxSe_2$ Based Solar Cells"
    42nd IEEE Photovoltaic Specialists Conference
    New Orleans, USA, June 14-19 2015.

16. T. Ashrafee, K. Aryal, G. Rajan, S. Karki, V. Ranjan, A. Rockett, R.W. Collins, S. Marsillac
"Effect of Substrate Temperature on Sputtered Molybdenum Film as a Back Contact for $Cu(In,Ga)Se_2$ Solar Cells"
42nd IEEE Photovoltaic Specialists Conference
New Orleans, USA, June 14-19 2015.

17. G. Rajan, K. Aryal, T. Ashrafee, S. Karki, A. Ibdah, V. Ranjan, R.W. Collins, S. Marsillac
"Optimization of Antireflective coatings for CIGS solar cells via Real Time Spectroscopic Ellipsometry"
42nd IEEE Photovoltaic Specialists Conference
New Orleans, USA, June 14-19 2015.

5. Budget and Schedule

- The project started on 09/01/11 and finished on 08/30/15

- The Project Budget was $1,117,402 from DOE and $338,194 as cost share

- The budget spent was $1,114,523.52 from DOE, $393,606 as cost share while $2,878.48 was unspent

- We requested a no-cost extension on May 2013 for the first budget period, due to challenges with equipment malfunction or unavailability. This request was granted.

- We requested a no-cost extension in December 2014 for the second budget period, to be able to achieve our deliverables. This request was granted.

6. Path Forward

Throughout our project, we have demonstrated that an integrated approach for enhancement of the device efficiency is critical, which entails working on modeling, characterization and fabrication in a synergistic manner, but also working on all layers of the devices.

In terms of characterization, we will continue pursuing in-situ and ex-situ ellipsometry as a new tool to enhance understanding of the deposition process, to guide future paths for deposition (new materials, new processes steps,..) but also to better understand existing devices via functionality such as mapping or tera-hertz technology.

In terms of layers, we have clearly demonstrated the potential for transition metal nitrides and transparent oxides, but still need to resolve the problem of the ohmicity of the contact and the enhanced shunt that occurs sometimes with these materials. We will continue focusing specifically on the oxide as they also present a path toward tandem cell as a transparent back contact. For the absorber layer, we will continue using RTSE to enhance the quality of the material, and see if we can understand better low temperature processes for CIGS, which present challenges similar to low thickness as the Gallium depth profile is drastically modified. Buffer layers are still very critical to understand. Recent results with KF treatment demonstrate that their thickness can be reduced, allowing for new research in this area. Finally, our enhanced modeling and understanding of AR filter will allow us to not only predict more reliably QE results based on optical properties, but also to idealize AR filters on any devices we fabricate even we modified absorber or buffer layer properties, which should allow for higher efficiency devices to be fabricated.

7. References

[1]   J. T. Heath and J. D. Cohen, W. N. Shafarman, D. X. Liao and A. A. Rockett, "Effect of Ga content on defect states in $CuIn_{l-x}Ga_xSe_2$ photovoltaic devices" American Institute of Physics (2002).

[2]   M. Igalsona, M. Edoff "Compensating donors in Cu(In,Ga)Sez absorbers of solar cells" Thin Solid Films 480-481 322-326, (2005).

[3]   W. Fucheng, T. Fuling, X. Hongtao, L. Wenjiang, F. Yudong, and R. Zhiyuan, "Effects of defect states on the performance of $CuInGaSe_2$ solar cells", Journal of Semiconductors, **35**, No. 2, (2014).

[4]   O. Lundberg, M. Bodegard, and L. Stolt, "Influence of the $Cu(In,Ga)Se_2$ thickness and Ga Grading on Solar Cell Performance", Prog. Photovolt: Res. Appl. 11, 77–88 (2003).

[5]   P. Jackson, D. Hariskos, R. Wuerz, O. Kiowski, A. Bauer,T. M. Friedlmeier, and M. Powalla,"Properties of Cu(In,Ga)Se2 solar cells with new record efficiencies up to 21.7%, Phys. Status Solidi RRL, 1–4 (2014).

[6]   K. Ramanathan, R. Noufi, B. To, D. L. Young, R. Bhattacharya, M. A. Contreras, R. G. Dhere, G. Teeter "Processing and Properties of Sub-Micron CIGS Solar Cells" in Conference Record of the 2006 IEEE 41h World Conference on PV, p. 380, (2006).

[7]   Bart Vermang et al. "Highly reflective rear surface passivation design for ultra-thin Cu(In,Ga)Se2 solar cells" Thin Solid Films 582 (2015) 300–303

[8]   Nathanaelle Schneider, Muriel Bouttemy, Pascal Genevée, Daniel Lincot and Frédérique Donsanti "Deposition of ultra thin CuInS2 absorber layers by ALD for thin film solar cells at low temperature (down to 150°C)" Nanotechnology 26 (2015) 054001

[9]   Claire van Lare, Guanchao Yin, Albert Polman, and Martina Schmid "Light Coupling and Trapping in Ultrathin Cu(In,Ga)Se2 Solar Cells Using Dielectric Scattering Patterns" ACS Nano 9(10) (2015) 9603-9613

[10]   G. Yin, V.Brackmann, V.Hoffmann, M.Schmid "Enhanced performance of ultra-thin Cu(In,Ga)Se2 solar cells deposited at low process temperature" Solar Energy Materials & Solar Cells 132 (2015) 142–147

[11]   A. Han, Y. Zhang,W. Song, B. Li,W. Liu and Y. Sun, "Structure, morphology and properties of thinned CIGS films and solar cells", Semicond. Sci. Technol. 27, 035022 (2012).

[12]   P. Jackson, D. Hariskos, E. Lotter et al., "New world record efficiency for $Cu(In,Ga)Se_2$ thin-film solar cells beyond 20%," Progress in Photovoltaics: Research and Applications, vol. 19, no. 7, pp. 894–897, (2011).